Three-Dimensional Modeling of Arc Voltage Fluctuations in Suspension Plasma Spraying

Elham Dalir

September 2016

Department of Mechanical and Industrial Engineering

Concordia University, Montreal, Quebec, Canada

Presented in Partial Fulfillment of the Requirements for the Degree of Master of Applied Science (Mechanical Engineering)

© Elham Dalir 2016

CONCORDIA UNIVERSITY
School of Graduate Studies

This is to certify that the thesis prepared

By: Elham Dalir

Entitled: Three-Dimensional Modeling of Arc Voltage Fluctuations in Suspension Plasma Spraying

and submitted in partial fulfillment of the requirements for the degree of

Master of Applied Science (Mechanical Engineering)

complies with the regulations of the University and meets the accepted standards with respect to originality and quality.

Signed by the final examining committee:

Dr. Ramin Sedaghati Chair

Dr. Marius Paraschivoiu Examiner

Dr. Fariborz Haghighat Examiner

Dr. Ali Dolatabadi and Dr. Christian Moreau Supervisor

Approved by _____
Chair of Department or Graduate Program Director

_____
Dean of Faculty

Date __

Abstract

Considering the wide range of plasma jet applications including plasma cutting, plasma spraying, and plasma arc waste disposal, realistic simulation of a plasma jet would significantly help to better understand and improve various processes. In this research, firstly a three-dimensional DC plasma torch is modeled using Joule effect method to simulate the plasma jet and its voltage fluctuations. The plasma gas is a mixture of argon/hydrogen and the arc voltage fluctuation is used as an input data in the model. Physical and chemical properties of plasma gases are used to model the plasma jet having high temperature and velocity. Reynolds Stress Model is used for time dependent simulation of the mixing flow of the plasma gas with atmosphere. After modeling the plasma jet, the results are applied to investigate the plasma oscillation effects on the trajectory, temperature, and velocity of suspension droplets. Suspensions are formed of ethanol and Yttria Stabilized Zirconia (YSZ, 8 wt.%) sub-micron particles and modeled as multicomponent droplets. To track the droplets and particles trajectory, a two-way coupled Eulerian-Lagrangian method is employed. In addition, in order to simulate the droplet breakup, Kelvin-Helmholtz Rayleigh-Taylor (KHRT) breakup model is used. After the completion of suspension breakup and evaporation, the spray particles are tracked through the domain to obtain the in-flight particle characteristics.

Keywords: Unsteady 3-D Simulation, Plasma Spray, Suspension Thermal Spraying, Yttria Stabilized Zirconia (YSZ)

Acknowledgments

Here I would like to express my gratitude and gratefulness towards Professor Ali Dolatabadi and Professor Christian Moreau for their support and assistance through this research. They have been nothing but kind and patient while guiding me through my masters. I have gained so much since I joined their exceptional research group at Concordia University.

I would also like to express my sincere thanks towards Mehdi Jadidi and Kourosh Pourang who have always helped me during my thesis.

At last, I want to thank my family for their love, patience, and support. Without their support, it was impossible for me to finish my master studies.

Table of contents

Abstract ..... **iii**

Acknowledgments ..... **iv**

List of Figures ..... **vii**

List of Tables ..... **x**

List of Symbols ..... **xi**

1 Introduction and Background **1**

1.1 Thermal Spray Coating Technology 2
1.2 Suspension Plasma Spraying (SPS) 4
1.3 Previous Studies 5
1.4 Motivation and Objectives 9

2 Methodology **11**

2.1 Continuous Phase Modeling 12
2.1.1 Governing Equations 12
Mass Conservation Equation 12
Momentum Conservation Equation 12
Energy Equation 13
Equation of State 13
Species Transport Equation 14
2.1.2 Turbulence Modeling 14
Reynolds Averaging 15
Reynolds Stress Model (RSM) 16

2.1.3 Near-Wall Treatments 17
Wall Functions 19
2.1.4 Numerical Schemes 20
2.2 Dispersed Phase Modeling 21
2.2.1 Particle Trajectory Equations 23
2.2.2 Particle Heat and Mass Transfer 23
2.2.3 Breakup Model Theory 25
Wave Breakup Model 27
2.3 Geometry and Computational Domain 29
2.4 Operating and Boundary Conditions 32
Plasma Heat Generation 34
SPS Modeling 36

3 Results and Discussion 38

3.1 Continuous Phase 39
3.1.1 Quasi- Steady Plasma Flow 39
3.1.2 Mesh Sensitivity Analysis 40
3.1.3 Transient Plasma Flow 41
3.2 Discrete Phase 46
3.2.1 Effect of Changing Suspension Feed Rate 56
3.2.2 Effect of Eliminating Voltage Fluctuations 63

4 Conclusion and Future Work 68

References 71

List of Figures

Figure 1.1- Schematic of a typical plasma spray gun 3

Figure 1.2- Classification of arc voltage fluctuation [5] 3

Figure 1.3- Phenomena involved in the radial suspension injection 5

Figure 2.1- Subdivisions of the near-wall region (Log-law region of velocity and wall shear stress data) [32] 18

Figure 2.2-Different near-wall treatments- (a) wall function approach, (b) near-wall model approach [32] 18

Figure 2.3- Solution algorithm of the pressure-based segregated Method [32] 21

Figure 2.4- Realistic mechanism of suspension droplet progress compared to the multicomponent theory [13] 22

Figure 2.5- Temperature based of zirconia particles specific heat [21] 22

Figure 2.6- Breakup regimes based on Weber number [37] 26

Figure 2.7- Liquid core length approximation [32] 27

Figure 2.8- 3MB plasma spray gun [38] 29

Figure 2.9- Geometry of domain of study and direction of inlet flow 30

Figure 2.10- Computational mesh of the domain of study 31

Figure 2.11- Finer mesh inside the plasma gun 31

Figure 2.12- Radiation losses versus temperature for argon/hydrogen mixture [27] 33

Figure 2.13- Arc voltage fluctuations- Ar_H2-(a) typical, (b) modeled with Fourier series34

Figure 2.14- Plasma torch with the heating zones $V1$ and $V2$ (quasi-steady) 35

Figure 2.15- Plasma torch with the heating zones $V1$ and $V2t$ 36

Figure 2.16- Schematic of injected droplets into the plasma jet 37

Figure 3.1- Plasma gas- (a) temperature and (b) velocity contours 40

Figure 3.2- Effect of the grid size on plasma gas- (a) temperature and (b) velocity..... 41

Figure 3.3- (a) Arc voltage of the saved data and (b) Used arc voltage fluctuations..... 42

Figure 3.4- Plasma gas temperature with a current input of 600A and arc voltage of (a) 62, (b) 50 and (c) 42 V..... 43

Figure 3.5- Plasma gas velocity with a current input of 600A and arc voltage of (a) 62, (b) 50 and (c) 42 V 43

Figure 3.6- Gas plasma temperature contours at a stand-off distance of 6 mm (4 snap shots)..... 44

Figure 3.7- Gas plasma velocity contours at a stand-off distance of 6 mm (4 snap shots) 45

Figure 3.8- Streamlines colored by plasma gas temperature and isosurface temperature of 11000 K with current input of 600 A and arc voltages of (a) 62, (b) 51 and (c) 42 V 46

Figure 3.9- Evolution of the temperature of a 25 μm particle as a function of time..... 47

Figure 3.10- Particle temperature and plasma gas temperature with a current input of 600 A and arc voltages of (a) 62, (b) 56 and (c) 46 V..... 49

Figure 3.11- Particle temperature and plasma gas temperature at 40 mm from the gun exit with arc voltages of $(a1)$ 62, $(a2)$ 56, and $(a3)$ 46 V and 60 mm from the gun exit with arc voltages of $(b1)$ 62, $(b2)$ 56, and $(b3)$ 46 V 51

Figure 3.12- Particle velocity and plasma gas velocity at 40 mm from the gun exit with arc voltages of $(a1)$ 62, $(a2)$ 56, and $(a3)$ 46 V and 60 mm from the gun exit with arc voltages of $(b1)$ 62, $(b2)$ 56, and $(b3)$ 46 V 52

Figure 3.13- Distribution of injected particle temperature, velocity, and size at a distance of 40 mm from the gun exit 54

Figure 3.14- Distribution of injected particle temperature, velocity, and size at a distance of 60 mm from the gun exit 55

Figure 3.15- Plasma gas and sprayed particles temperatures with suspension feed rates of (a) 22, (b) 32, and (c) 42 g/min 57

Figure 3.16- Plasma gas and sprayed particles temperatures with suspension feed rates of (a) 22, (b) 32, and (c) 42 g/min at a distance of 40 mm from the gun exit .. 58

Figure 3.17- Plasma gas and sprayed particles velocities with suspension feed rates of (a) 22, (b) 32, and (c) 42 g/min at a distance of 40 mm from the gun exit 59

Figure 3.18- Particles temperature located at a distance of 40 mm from the gun exit with feed rates of (a) 22, (b) 32, and (c) 42 g/min 60

Figure 3.19- Particles velocity located at a distance of 40 mm from the gun exit with feed rates of (a) 22, (b) 32, and (c) 42 g/min 61

Figure 3.20- Particles diameter located at a distance of 40 mm from the gun exit with feed rates of (a) 22, (b) 32, and (c) 42 g/min 62

Figure 3.21- Windward trajectory of injected particles with mass flow rates of 22, 32, and 42 g/min 63

Figure 3.22- Windward trajectory of injected particles in two cases of swirl without voltage fluctuations and swirl with voltage fluctuations (suspension mass flow rate is 22 g/min) 64

Figure 3.23- Particles temperature located at a distance of 40 mm from the gun exit (a) swirl with voltage fluctuations, (b) swirl without voltage fluctuations 65

Figure 3.24- Particles velocity located at a distance of 40 mm from the gun exit (a) swirl with voltage fluctuations, (b) swirl without voltage fluctuations 66

Figure 3.25- Particles diameter located at a distance of 40 mm from the gun exit (a) swirl with voltage fluctuations, (b) swirl without voltage fluctuations 67

List of Tables

Table 2.1- Operating condition for plasma spraying simulation..... 32

Table 2.2- Coefficients of modeled voltage fluctuations function..... 34

Table 2.3- Material thermos-physical properties [21], [39]..... 37

List of Symbols

$\boldsymbol{C_D}$	Drag coefficient	
$\boldsymbol{C_p}$	Particle specific heat	[J/kg.K]
$D_{i,m}$	Diffusion coefficient	[m^2/s]
d_p	Particle diameter	[m]
$\boldsymbol{F}$	External body force	[N]
F_D	Drag force	[N]
$\boldsymbol{g}$	Gravitational acceleration	[m/s^2]
I	Unit tensor	
k	Thermal conductivity	[W/m.K]
L	Flow characteristic length	[m]
M	Average molecular mass	[mass/mole]
m	Average molecular mass	[kg]
Ma	Mach number	

Nu	Nusselt number	
p	Pressure	[Pa]
Pr	Prandtl number	
$\dot{\boldsymbol{q}}$	Heat flux	[W/m^2]
R	Specific gas constant	[J/kg.K]
R_0	Universal gas constant	[J/kg.K]
Re	Reynolds number	
t	time	[s]
T	Temperature	[K]
$\vec{\boldsymbol{u}}$	Fluid velocity vector	[m/s]
$\vec{\boldsymbol{u}}_{\boldsymbol{p}}$	Particle velocity vector	[m/s]
V	Volume	[m^{-3}]
μ	Dynamic viscosity	[kg/m.s]
ρ	Density	[kg/m^3]
$\bar{\bar{\boldsymbol{\tau}}}$	Stress tensor	

υ	Kinematic viscosity	[m^2/s]

1 Introduction and Background

Overview

In this chapter, a summarized introduction of the thermal spray technology and the suspension plasma spraying technique will be given. In addition, the current study motivation and objectives will be discussed.

1.1 Thermal Spray Coating Technology

For many years, the thermal spray coating technology has been increasingly used in many fields such as aerospace, automotive, chemistry, etc. Producing more resistant surfaces against corrosion, applying higher temperature exposure in the thermal barrier coatings or extending the lifetime of surface properties by recreating the worn parts instead of replacing the whole component are few examples of enhancing the functional performance of the structural parts in different applications [1]. In thermal spraying, metallic or non-metallic materials are injected into a high temperature and high speed jet to obtain molten or semi-molten condition to form protecting coatings [2].

Based on the methods applied to provide the required energy to melt the sprayed materials, thermal spray is divided by combustion, electrical discharge, or high-pressure gases in the case of cold spraying [1]. Among different types of thermal spray processes, plasma spraying is mostly used. The plasma working gases injected into the torch are heated by the arc struck between the cylindrical copper anode and the tungsten cathode producing a high velocity and high temperature plasma jet. The plasma working gas could be a single gas (e.g. Ar) or a mixture of a primary gas (Ar or N2) and a secondary gas (H_2, He) to improve heat and momentum transfer to the spray particles (Ar-H_2, Ar-He, Ar-He-H_2, etc.) [1]. Figure 1.1 shows different parts of a plasma spray process which are the cathode region, the arc column region, and the anode region. Based on the torch operating condition, the plasma jet velocity and temperature at the gun exit could reach 2000 m/s and 14000 K, respectively [3]. The material to be deposited is normally injected at the exit of the plasma torch in the form of powders whose size ranges typically between 10 to 80 μm. The injected particles are heated and accelerated towards the substrate where they impact, flatten and solidify to form a coating.

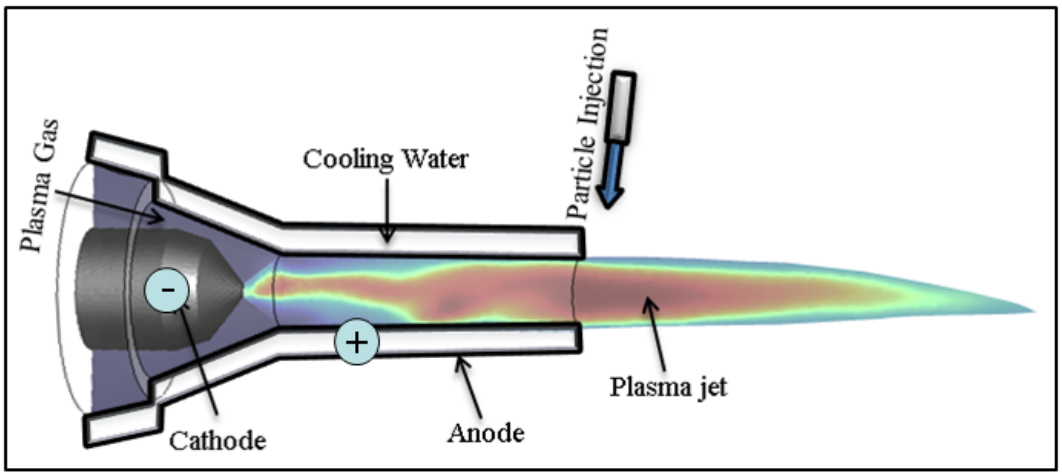

Figure 1.1- Schematic of a typical plasma spray gun

An important instability in DC plasma spray is the arc voltage fluctuation which is classified in three different modes: Steady mode in which the voltage fluctuation is negligible; Takeover mode which introduces the arc oscillations as a quasi-periodic motion; and the Restrike mode which shows a highly unstable plasma jet motion as a result of large arc voltage fluctuations [4]. Figure 1.2 illustrates the arc voltage classification.

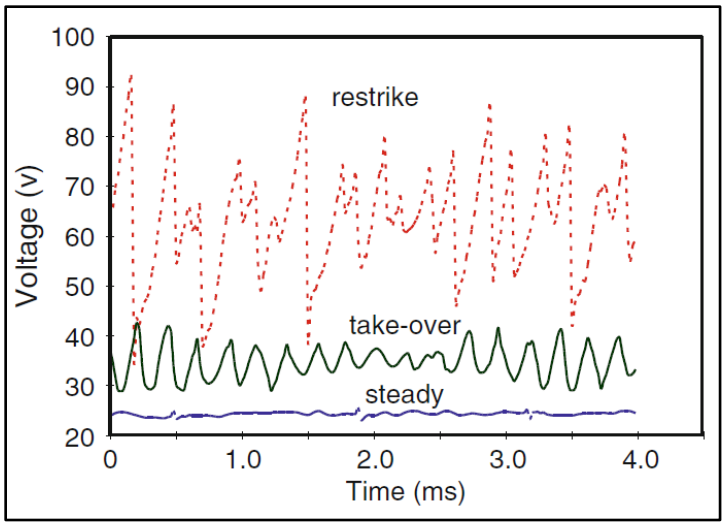

Figure 1.2- Classification of arc voltage fluctuation [5]

In plasma spray applications, it is desirable to achieve stable operating conditions. The unmelted particles and the poor coating quality would be the results of oscillations in the plasma jet temperature [6]. Because of the significant effects of the arc voltage fluctuations on the suspension plasma spraying (SPS) properties, the focus of this study is to model the plasma jet inside and outside the torch considering the arc voltage fluctuations.

1.2 Suspension Plasma Spraying (SPS)

To have a proper surface coating of sub-micron and nano-sized particles, a relatively new deposition process, suspension plasma spraying (SPS), has been increasingly used. In the SPS technique, submicron and nano-sized particles are sprayed efficiently to form finely structured coatings [7-9]. To have enough momentum for the fine particles to penetrate into the plasma jet, a liquid carrier feedstock (e.g. ethanol or water) is necessary. The suspension droplets penetration occurs when their momentum density ($\rho_l v_l^2$) is higher than that for the gas flow ($\rho_g v_g^2$). Particles are injected inside or outside the plasma torch in axial or radial types considering the plasma jet direction. The type and the location of the particle injection have a major effect on the particles properties such as trajectory, temperature, and velocity [10].

Based on several studies, liquid fragmentation occurs when the Weber number, the ratio of the aerodynamic force to the surface tension force, becomes more than 14 [11]. The ideal result is when all particles injected into the plasma flow reach the substrate with a temperature well above their melting point and below their vaporization point with high enough velocities to actually impact on the substrate surface [12]. Therefore, a critical aspect in the SPS process is to well control the suspension droplets trajectories, temperatures, velocities, and their interactions with the plasma flow. Suspension transport into the plasma flow shown in Figure 1.3, is a very complex phenomenon.

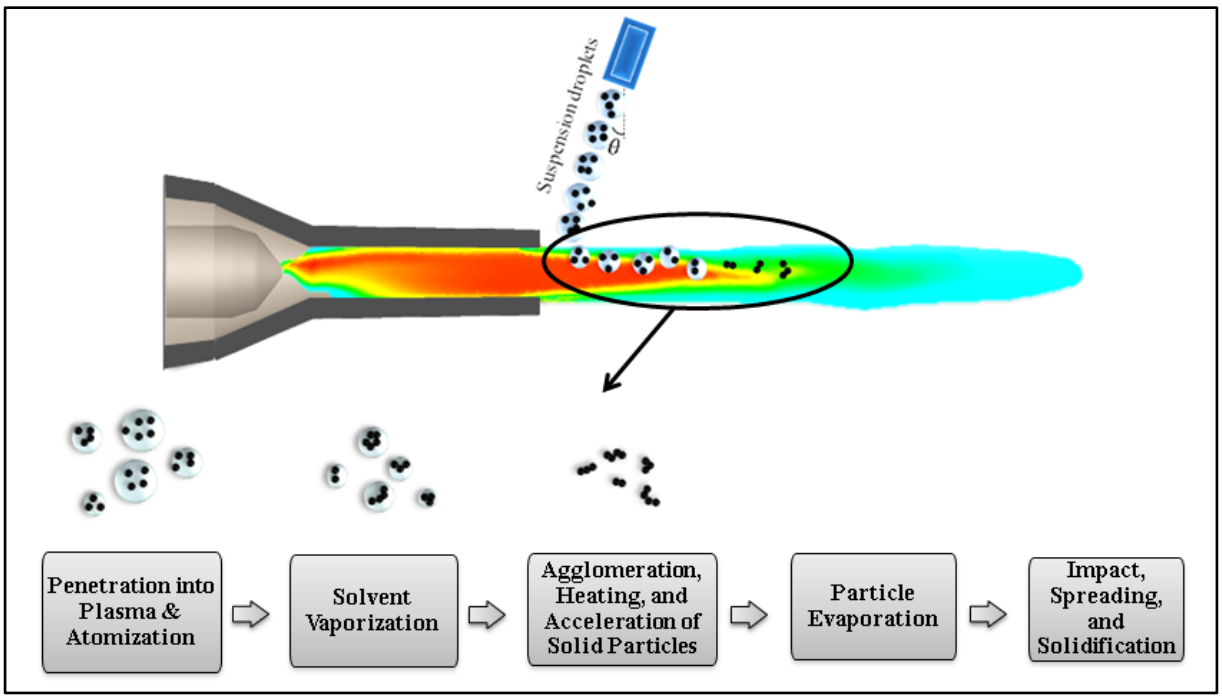

Figure 1.3- Phenomena involved in the radial suspension injection

As soon as suspension droplets reach the plasma flow, first the liquid is fragmented into the dispersed droplets, then the droplets are vaporized and finally solid particles are melted, accelerated toward the substrate and the splats are formed. Compared to the conventional spraying, the plasma arc voltage fluctuations have a more significant effect on the particles penetration, fragmentation, trajectories, heating, and acceleration in the suspension spraying. Thus, modeling the plasma jet with its oscillations is crucial to have more accurate results.

1.3 Previous Studies

Considering the high volume of plasma jet applications including plasma cutting, plasma spraying, and plasma arc waste disposal, realistic simulation of a plasma jet would significantly help to better understand and improve various processes. Due to the nature of the plasma jet and its attachment on the anode surface, the arc experiences important fluctuations which results in large arc voltage fluctuations that should be considered in the simulations.

There are several numerical approaches used in order to simulate the plasma jet. In one approach, the plasma jet is considered to be steady, and temperature and velocity profiles are used as the input data [13-20]. In another approach, a constant volumetric heat source located inside the torch is added to the energy equation to generate the plasma heat. In this approach, the plasma jet is still in the steady state [21-22].

Based on the fact that the plasma jet formation is naturally an unsteady phenomenon, the results obtained from the steady simulations may not be able to capture the unsteady features of flow inside and outside the torch. There are two main effective methods used to simulate the transient plasma jet as explained below.

The first approach is based on coupling the fluid mechanics and electromagnetic equations to model the plasma jet [23-26]. Moreau et al. [26] used a three-dimensional transient model with the nozzle diameter of 7 mm to simulate the oscillating plasma jet. The plasma working gases was $Ar - H_2$ and the voltage fluctuation was in the restrike mode due to the torch operating condition. To simulate the anode root attachment inside the torch, the electromagnetic equations in addition to the mass, momentum, and energy equations were applied. The effect of changing the arc current was investigated in this study and the results showed a higher maximum velocity at the nozzle exit due to increase in the arc current. A higher voltage fluctuation frequency was also predicted with the arc current increasing.

The second approach, which is used in the current study, is modeling the plasma jet based on the Joule effect method [27]. Meillot et al. [27] simulated a three-dimensional D.C plasma gun by introducing a time-dependent volumetric heat source inside the plasma torch. The validation criterion was the thermal efficiency through adjusting the length of the plasma column inside the

torch and the results of the centerline plasma jet properties especially near the gun exit were in agreement with the experiments.

Generating a coating with a good quality requires a detailed understanding of the plasma jet and its interaction with the injected particles. Arc voltage fluctuations, particle mass flow rate, injector angle and particle size distribution are some of the effective parameters in plasma spraying process. Arc voltage fluctuations cause a poor control on the heat and momentum transfer between the oscillating plasma jet and the injected particles. Using different types of plasma gases such as $Ar - H_2$ and the anode erosion has significant effects on the arc oscillations.

Duan [28] investigated the effect of the anode erosion on the oscillating plasma jet by using a SG-100 plasma torch with the arc current of 500 A and the mixture of argon/helium as the plasma forming gases with a swirl injector. Under such operating conditions, the takeover mode was dominant. The results illustrated that the mean arc voltage decreases with the increasing anode erosion, while the plasma jet instability increases.

Since the plasma flow inside and outside the plasma gun is a turbulent flow, it is necessary to find and apply the proper turbulent model which gives more accurate results specially in the case of having injected suspension. In most studies, an Eulerian-Lagrangian approach is used to simulate the suspension droplets interaction with the plasma flow. The details of the mentioned approach and the turbulence models will be discussed in the next chapter.

Remesh et al. [29] investigated the effects of changing the carrier gas flow rate on the particles characteristics. In their study, a three-dimensional modeling was used to simulate an $Ar - H_2$ plasma gas with yttria-stabilized zirconia (YSZ) as the sprayed particles. It was found that by increasing the carrier gas flow rate from 2 to 4 slm, the average value of particles

temperature and velocity are increased by 10% and 16%, respectively. It was also shown that when the carrier gas flow rate increases to 6 slm, particles temperature do not change, while particles velocity decrease by 20%.

Shan et al. [30] used Re-Normalization Group (RNG) $k-\varepsilon$ turbulent model in a 3D plasma spray modeling to simulate the plasma jet. To model the droplet breakup and collision, Taylor Analogy Breakup (TAB) and O'Rourke's models were used, respectively. In their study, the effects of droplet collision and breakup on the particle characteristics were investigated. The results showed that the droplet collision causes an increase in the average size of the particles while the droplet breakup plays an important role in the reduction of the average droplet size.

Vincent et al. [31] used a numerical simulation of the interaction between the plasma flow and injected water jet using LES turbulent model and volume of fluid (VOF) method to simulate the plasma flow and primary breakup (fragmentation) of the droplet, respectively. The validation was done successfully in an argon plasma flow and a good agreement compared to the experiments was obtained in the mean temperature and velocity profiles.

The main trend is to use suspension plasma spraying which is an emerging process to create submicron- and nanostructured coatings with enhanced properties. Jabbari et al. [13] modeled the suspension plasma spraying using nickel powder and ethanol as the solvent. Suspension droplets were injected radially into a 3MB Sulzer plasma gun and simulated as the multicomponent droplets. The arc fluctuations were neglected and the plasma gas was argon. RSM model was utilized to simulate the plasma gas and its interaction with the sprayed particles. However, the authors also applied k-ε model in the free plasma jet to compare the results with the results of RSM turbulent model. It was shown that the k-ε model gives underestimated values for the high temperature plasma core. To model the particle secondary breakup, KHRT breakup model which

gives reasonable results in the case of high Weber number was used. It was concluded that by increasing the suspension injection velocity, the penetration depth increases and when the injection velocity is too high, the quantity of the particles with high temperature decreases.

Jadidi et al. [14] analyzed the effect of using a flat substrate with the same conditions and assumptions used in [13] in SPS process. The effect of the standoff distance on particles properties upon impact in the vicinity of the substrate was investigated. It was shown that many fine particles were diverted due to the stagnation region formed near the substrate. It was also concluded that particles moving near the plasma gas centerline obtain higher velocity and higher temperature and are less affected by the stagnation region.

Recently the effect of curved substrates on the suspension droplet characteristics especially near the substrate was investigated by Pourang et al. [21]. The authors applied the assumptions used in [13]. However, in order to improve the simulation of the high velocity and the high temperature plasma gas, a constant volumetric energy source $\left(\frac{\eta_t EI}{V}\right)$ was introduced inside the torch and added to the energy equation. The suspension contained zirconia particles (10 wt.%) and ethanol as the solvent and modeled as the multicomponent droplets. The results showed that the finer particles obtain higher temperature and velocity compared to other particles. It was also found that compared to the use of flat substrate, the deposition rate decreases more than 50 % on a cylindrical substrate.

1.4 Motivation and Objectives

The principal aim in this study is to obtain a more realistic prediction of plasma jet considering arc oscillations, and the interaction between the suspension droplets and the fluctuating plasma jet to achieve controllable and repeatable suspension spraying properties. To achieve this goal, a three-dimensional numerical model is used to simulate the arc fluctuations.

In addition, different suspension feed rates are injected into the plasma gas to investigate the effect of the plasma oscillations on the particles properties. The current study objectives are listed as:

1- Modeling the transient plasma jet by using the arc voltage fluctuations.
2- Simulating the suspension injection and its interaction with the transient plasma flow considering the penetration, fragmentation, solvent evaporation and melting of spray particles.
3- Investigating the effect of using different suspension feed rates on the particles properties.

2 Methodology

Overview

To model the plasma spray coating, an Eulerian- Lagarangian method explained in details in this chapter is used. The Eulerian approach is used to model the continuous phase (plasma jet) and Lagrangian approach is applied to simulate the discrete phase (suspension droplets and particles).

2.1 Continuous Phase Modeling

Since the plasma jet is unsteady in nature and its fluctuations have effects on the suspension injection properties, the focus of this study is to model the arc fluctuations of a DC plasma jet using the assumptions which can capture the nature of this unsteady multiphase flow.

2.1.1 Governing Equations

To model all kinds of flows, mass and momentum conservation equations should be solved. However, energy and species conservation equations also should be solved in the cases of having heat transfer or compressibility and mixing of species, respectively.

Mass Conservation Equation

The general form of mass conservation equation or continuity equation, which can be used for both incompressible and compressible flows, is written as [32],

$$\frac{\partial \rho}{\partial t} + \nabla.(\rho \vec{v}) = S_m \tag{2-1}$$

where S_m is the source of mass added to the continuous phase from the dispersed second phase such as the vaporization of the droplets or any other user-defined sources.

Momentum Conservation Equation

Conservation of momentum is employed by [32],

$$\frac{\partial}{\partial t}(\rho \vec{v}) + \nabla.(\rho \vec{v}\vec{v}) = -\nabla p + \nabla.(\bar{\bar{\tau}}) + \rho \vec{g} + \vec{F} \tag{2-2}$$

where p is the static pressure, $\bar{\bar{\tau}}$ is the stress tensor, $\rho \vec{g}$ is the gravitational body force, and $\vec{F}$ is the external body forces. The stress tensor, $\bar{\bar{\tau}}$, is given by,

$$\bar{\bar{\tau}} = \mu \left[(\nabla \vec{v} + \nabla \vec{v}^T) - \frac{2}{3} \nabla.\vec{v} I \right] \tag{2-3}$$

where μ is the molecular viscosity, I is the unit tensor, and the second term on the right hand side is the effect of volume dilation.

Energy Equation

The energy equation is solved using the following equation [32],

$$\frac{\partial}{\partial t}(\rho E) + \nabla.\left(\vec{v}(\rho E + p)\right) = \nabla.\left(k_{eff}\nabla T - \sum_j h_j \vec{J_j} + \left(\bar{\bar{\tau}}_{eff}.\vec{v}\right)\right) + S_h + S_{rad} \quad (2\text{-}4)$$

where, k_{eff} is the effective conductivity and $\vec{J_j}$ is the diffusion flux of species j. The terms on the right-hand represent the conduction energy transfer, species energy transfer, and viscous dissipation energy transfer, respectively. S_h is the volumetric heat source added to the model, and S_{rad} represents the heat losses due to radiation. E is calculated as,

$$E = h - \frac{p}{\rho} + \frac{v^2}{2} \quad (2\text{-}5)$$

In this research, to account for the arc plasma heating, the volumetric heat source, S_h, from equation (2-4) is computed from the following equation,

$$S_h = \frac{EI}{V} \quad (2\text{-}6)$$

where, E is the arc voltage (V), I is the arc current (A), and V is the volume of the column inside anode. Equation (2-6) and its application is explained in details later in this study.

Equation of State

The following equation, called equation of state for ideal gas, is used to close the system of the above mentioned equations,

$$p = \rho R T \quad (2\text{-}7)$$

$$R = \frac{R_0}{M} \quad (2\text{-}8)$$

where R is the specific gas constant for the gas under consideration, R_0 is the universal gas constant, and M is the average molecular mass ($mass/mole$).

Species Transport Equation

In cases of solving the chemical species' conservation equations, the local mass fraction of each species, Y_i, using the solution of a convection-diffusion equation for the ith species is predicted as [32],

$$\frac{\partial}{\partial t}(\rho Y_i) + \nabla.(\rho \vec{v} Y_i) = -\nabla.\vec{J_i} + R_i + S_i \tag{2-9}$$

where R_i is the net rate of production of species i by chemical reaction (in this study $R_i = 0$) and S_i is the rate of creation by addition from the dispersed phase plus any user-defined sources. Equation (2-9) is solved for $N - 1$ species where N is the total number of fluid phase chemical species.

2.1.2 Turbulence Modeling

The gas flow in a DC plasma spray torch is turbulent with high temperature and velocity gradients. Thus, choosing a turbulent model which is appropriate to simulate the arc fluctuations and to predict the plasma core length correctly is very important in this study. The Large Eddy Simulation (LES) model is a powerful tool to study turbulent flow structure where large eddies are directly solved and small eddies are modeled which are less geometry-dependent [31]. Due to the high computational costs associated with LES solvers, RNG k-ε and RSM models have been widely used and showed a better prediction of the particle parameters [16] and the plasma core length [13] compared to the standard k-ε model, respectively.

Reynolds Averaging

The variables of the exact Navier-Stokes equations in Reynolds averaging are calculated from the time-averaged and fluctuating components [32],

$$\emptyset = \overline{\emptyset} + \emptyset' \tag{2-10}$$

where, $\emptyset$ denotes a scalar quantity such as pressure, energy, or species concentration. For the velocity components, it is written as,

$$u_i = \bar{u}_i + u_i{}' \tag{2-11}$$

where, $\bar{u}_i$ and $u_i{}'$ are the mean and fluctuating velocity components.

Substituting equation (2-11) into the continuity and momentum equations and taking a time average gives the ensemble-averaged momentum equations called Reynolds-averaged Navier-Stokes equations,

$$\frac{\partial \rho}{\partial t} + \frac{\partial}{\partial x_i}(\rho u_i) = 0 \tag{2-12}$$

$$\frac{\partial}{\partial t}(\rho u_i) + \frac{\partial}{\partial x_j}(\rho u_i u_j) = -\frac{\partial p}{\partial x_i} + \frac{\partial}{\partial x_j}\left[\mu\left(\frac{\partial u_i}{\partial x_j} + \frac{\partial u_j}{\partial x_i} - \frac{2}{3}\delta_{ij}\frac{\partial u_l}{\partial x_l}\right)\right] + \frac{\partial}{\partial x_j}\left(-\rho\overline{u_i' u_j'}\right) \tag{2-13}$$

where $-\rho\overline{u_i' u_j'}$, Reynolds stresses, represent the effects of the turbulence. To use the Reynolds-averaged approach, the Reynolds stresses should be modeled properly. In a common approach, the Boussinesq hypothesis is used to model the Reynolds stresses,

$$-\rho\overline{u_i' u_j'} = \mu_t\left(\frac{\partial u_i}{\partial x_j} + \frac{\partial u_j}{\partial x_i}\right) - \frac{2}{3}\left(\rho k + \mu_t\frac{\partial u_k}{\partial x_k}\right)\delta_{ij} \tag{2-14}$$

where μ_t is the turbulent viscosity and k is the turbulence kinetic energy. The advantage of using this approach is the lower computational cost due to the turbulent viscosity computation. The Boussinesq hypothesis is used in $k - \varepsilon$ and the $k - \omega$ models to model the Reynolds stresses.

Reynolds Stress Model (RSM)

Reynolds Stress Model (RSM) is an alternative to the Boussinesq hypothesis in which the terms of Reynolds stress tensor are solved using the transport equations. The transport equations for the Reynolds stresses transport, $\rho\overline{u_i'u_j'}$, are written as [32],

$$\underbrace{\frac{\partial}{\partial t}\left(\rho\overline{u_i'u_j'}\right)}_{Local\ Time\ Derivative} + \underbrace{\frac{\partial}{\partial x_k}\left(\rho u_k\overline{u_i'u_j'}\right)}_{C_{ij}\equiv Convection} = \underbrace{-\frac{\partial}{\partial x_k}\left[\rho\overline{u_i'u_j'u_k'} + \overline{p'\left(\delta_{kj}u_i' + \delta_{ik}u_j'\right)}\right]}_{D_{T,ij}\equiv Turbulent\ Diffusion} +$$

$$\underbrace{\frac{\partial}{\partial x_k}\left[\mu\frac{\partial}{\partial x_k}\left(\overline{u_i'u_j'}\right)\right]}_{D_{L,ij}\equiv Molecular\ Diffusion} \underbrace{-\rho\left(\overline{u_i'u_k'}\frac{\partial u_j}{\partial x_k} + \overline{u_j'u_k'}\frac{\partial u_i}{\partial x_k}\right)}_{P_{ij}\equiv Stress\ Production} + \underbrace{\overline{p'\left(\frac{\partial u_i'}{\partial x_j} + \frac{\partial u_j'}{\partial x_i}\right)}}_{\phi_{ij}\equiv Pressure\ Strain} - \underbrace{2\mu\overline{\frac{\partial u_i'}{\partial x_k}\frac{\partial u_j'}{\partial x_k}}}_{\varepsilon_{ij}\equiv Dissipation} +$$

$$\underbrace{S_{user}}_{User-Defined\ Source\ term} \qquad (2\text{-}15)$$

Turbulence kinetic energy is obtained from,

$$k = \frac{1}{2}\overline{u_i'u_j'} \qquad (2\text{-}16)$$

In order to close the Reynolds-averaged Navier-Stockes equations, an equation for the dissipation tensor is needed which is modeled as,

$$\varepsilon_{ij} = \frac{2}{3}\delta_{ij}(\rho\varepsilon + Y_M) \qquad (2\text{-}17)$$

where $Y_M = 2\rho\varepsilon M_t^2$, M_t is the Mach number and is defined as,

$$M_t = \sqrt{\frac{k}{a^2}} \qquad (2\text{-}18)$$

where a is the speed of sound $\left(\sqrt{\gamma RT}\right)$. The scalar dissipation rate, ε, is computed using a transport equation similar to the one applied in $k-\varepsilon$ model,

$$\frac{\partial}{\partial t}(\rho\varepsilon) + \frac{\partial}{\partial x_i}(\rho\varepsilon u_i) = \frac{\partial}{\partial x_j}\left[\left(\mu + \frac{\mu_t}{\sigma_\varepsilon}\right)\frac{\partial\varepsilon}{\partial x_i}\right] C_{\varepsilon 1}\frac{1}{2}P_{ii}\frac{\varepsilon}{k} - C_{\varepsilon 2}\rho\frac{\varepsilon^2}{k} + S_\varepsilon \qquad (2\text{-}19)$$

where $\sigma_\varepsilon = 1.0$, $C_{\varepsilon 1} = 1.44$, and $C_{\varepsilon 2} = 1.92$. The turbulent viscosity, μ_t, in RSM is obtained similarly to the $k-\varepsilon$ model,

$$\mu_t = \rho C_\mu \frac{k^2}{\varepsilon} \tag{2-20}$$

where $C_\mu = 0.09$.

2.1.3 Near-Wall Treatments

In turbulent flow cases, the flow is significantly affected by the existing walls with the no-slip boundary condition. Very close to the wall, flow is laminar and by going far from the wall, it changes to turbulent flows. Therefore, the near-wall modeling in the numerical solutions of turbulent flows is very important.

Numerous experiments have been done to find the applicable results to model the turbulent flows near the walls. One of the applicable results extracted from a wide variety of boundary layers in turbulent flow cases is plotted in semi-log coordinates in Figure (2.1). Based on this plot with dimensionless velocity data, flow in the innermost layer, "viscous sublayer", is almost laminar. In viscous sublayer, the most dominant parameter in momentum and heat or mass transfer equations is the molecular viscosity. Between the viscous sublayer ($y^+ \approx 5$) and the outer layer which is fully turbulent layer, both molecular and turbulence viscosities have effect on the flow. In the outer layer shown in Figure 2.1, turbulence viscosity plays the major role [32].

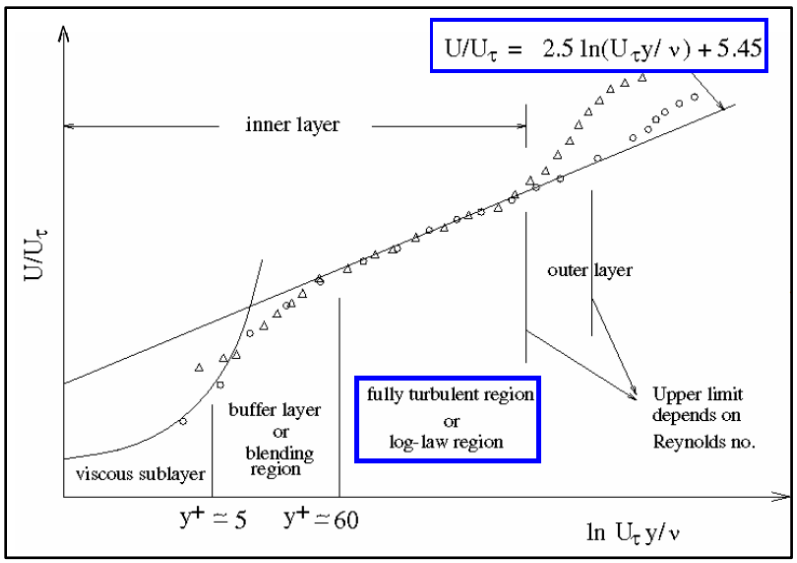

Figure 2.1- Subdivisions of the near-wall region (Log-law region of velocity and wall shear stress data) [32]

Generally there are two approaches to model the near-wall region. In one approach, called "wall functions", the viscosity affects the viscous sublayer and the buffer layer is not resolved. In this approach, semi-empirical formulas are used to connect the viscosity between the wall and the fully-turbulent region.

In the other approach, called "near-wall model", the turbulence models are modified to resolve the viscosity in the inner layer (viscous sublayer and buffer layer). In this method, $y^+ \approx 1$ and finer mesh near the wall is required to resolve the viscous sublayer. Figure 2.2 shows the concept of the two mentioned methods.

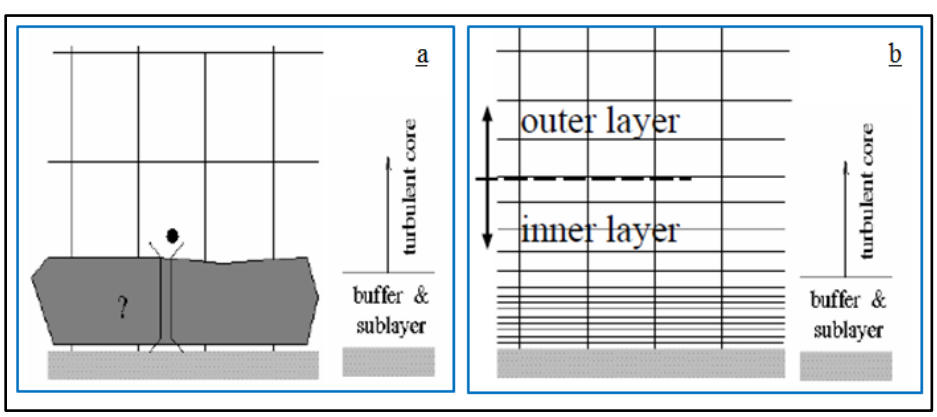

Figure 2.2-Different near-wall treatments- (a) wall function approach, (b) near-wall model approach [32]

Since near-wall model is usually applied in low-Re flows or flows with complex near-wall phenomena, and also to be able to use coarser mesh near the wall region, the wall function approach is used in the current study.

Wall Functions

The law-of-the-wall for mean velocity is calculated [32],

$$\begin{cases} U^* = \frac{1}{k} ln(Ey^*) & y^* > 11.225 \\ U^* = y^* & y^* < 11.225 \end{cases} \tag{2-21}$$

where k is von Karman constant (0.4187), E is empirical constant (9.793), U^* is the dimensionless velocity, and y^* is the dimensionless distance from the wall. U^* and y^* are calculated from equations (2-24) and (2-25),

$$U^* = \frac{U_p C_\mu^{1/4} k_p^{1/2}}{\tau_w/\rho} \tag{2-22}$$

$$y^* = \frac{\rho C_\mu^{1/4} k_p^{1/2} y_p}{\mu} \tag{2-23}$$

where, U_p is the mean velocity of the fluid at the near-wall node *P,* k_p is the turbulence kinetic energy at the near-wall node *P,* y_p is the distance from point *P* to the wall, and μ is the dynamic viscosity of the fluid.

Reynolds's analogy between the momentum and energy transport gives a similar logarithmic law for mean temperature,

$$T^* \equiv \frac{(T_w - T_P)\rho c_p C_\mu^{\frac{1}{4}} k_P^{\frac{1}{2}}}{\dot{q}} = \begin{cases} Pry^* + \frac{1}{2}\rho Pr \frac{C_\mu^{\frac{1}{4}} k_P^{\frac{1}{2}}}{\dot{q}} U_P^2 & y^* < y_T^* \\ Pr_t \left[\frac{1}{k} ln(Ey^*) + P\right] + & \\ \frac{1}{2}\rho \frac{C_\mu^{\frac{1}{4}} k_P^{\frac{1}{2}}}{\dot{q}} \{Pr_t U_P^2 + (Pr - Pr_t) U_C^2\} & y^* > y_T^* \end{cases} \tag{2-24}$$

where P is computed as,

$$P = 9.24\left[\left(\frac{Pr}{Pr_t}\right)^{3/4} - 1\right]\left[1 + 0.28e^{-0.007Pr/Pr_t}\right] \tag{2-25}$$

where k_P is the turbulent kinetic energy at the first near-wall node P, ρ is the fluid density, c_p is the specific heat of fluid, $\dot{q}$ is the wall heat flux, T_P is the temperature at the first near-wall node P, T_w is the temperature at the wall, Pr is the molecular Prandtl number, Pr_t is the turbulent Prandtl number (0.85 at the wall), and U_C is the mean velocity magnitude at $y^* = y_T^*$.

2.1.4 Numerical Schemes

In the pressure-based approach, the pressure field is calculated from solving a pressure correction equation obtained from continuity and momentum equations. This approach uses a control-volume-based technique by dividing the domain into discrete control volumes using a computational grid to solve the governing equations for mass, momentum, energy, and other scalars [32].

In the pressure-based method, a solution algorithm called pressure-based segregated in which the governing equations are solved segregated from one another is used. This method is memory-efficient due to storing the discretized equations in the memory one at a time. Figure 2.3 shows the pressure-based segregated algorithm [32]. In this study, the pressure-based approach with a second-order upwind scheme is used to compute the flow properties at the cell faces.

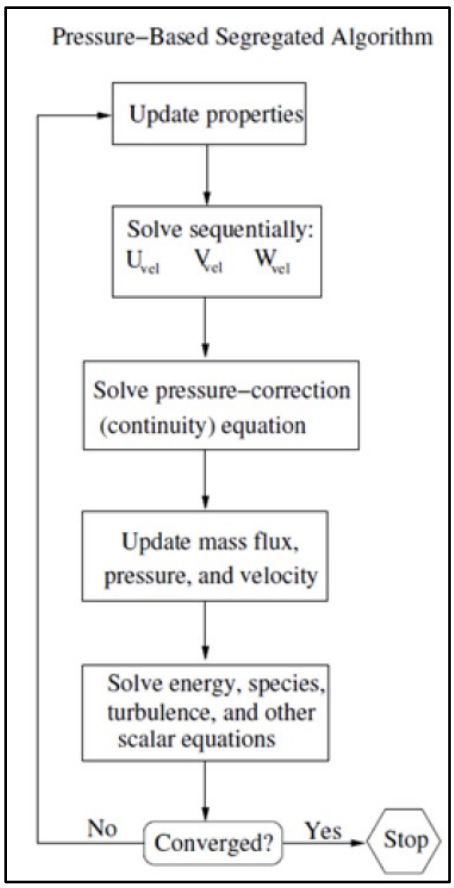

Figure 2.3- Solution algorithm of the pressure-based segregated Method [32]

2.2 Dispersed Phase Modeling

After modeling the plasma jet, the converged results are used to investigate the plasma oscillation effects on the trajectory, temperature, and velocity of the injected suspension droplets. Suspension droplets are formed of ethanol and Yttria Stabilized Zirconia (YSZ, 8 wt.%) sub-micron particles and modeled as multicomponent droplets. Figure 2.4 shows the real suspension droplet progress and the multicomponent droplets used in this model [13]. Suspension droplets start to break up and then evaporate as soon as they interact with the continuous phase (plasma jet). A Lagrangian approach including coupling with the continuous phase is used for the discrete phase modeling.

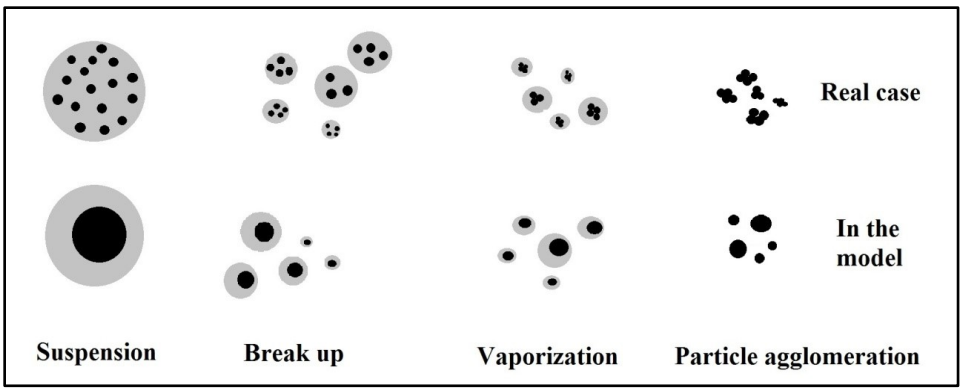

Figure 2.4- Realistic mechanism of suspension droplet progress compared to the multicomponent theory [13]

The specific heat of the zirconia particles during melting is calculated as [21],

$$C_p \times \Delta T = H_f \tag{2-26}$$

where C_p is the particle specific heat, and H_f is the particle fusion enthalpy. Figure 2.5 shows the applied method in which ΔT is assumed to be 10 K.

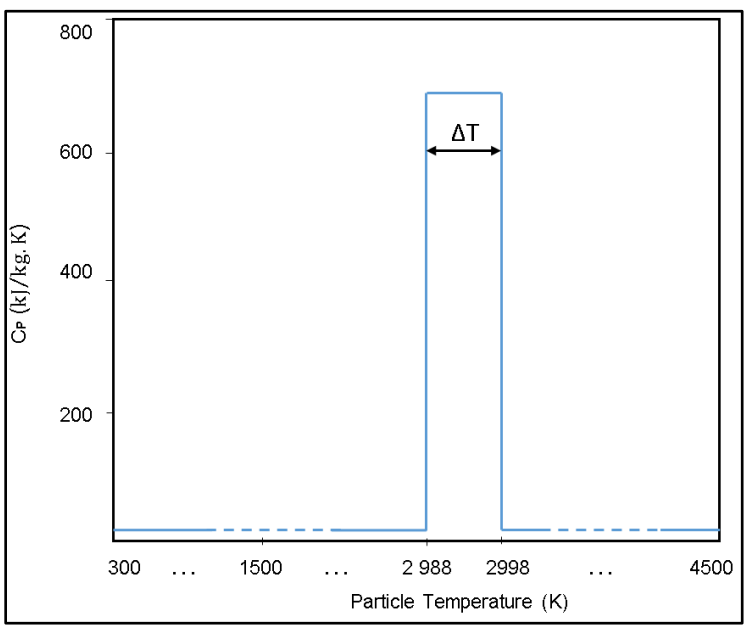

Figure 2.5- Temperature based of zirconia particles specific heat [21]

To predict the particle dispersion due to the fluid phase turbulence, a model called the stochastic tracking model is used. This model which is a random walk model is applied by including the instantaneous turbulent velocity fluctuations on the particle trajectories.

2.2.1 Particle Trajectory Equations

The particle (or droplet) trajectory is predicted by integrating the force balance on the particle [32],

$$\frac{du_p}{dt} = F_D\left(\vec{u} - \vec{u}_p\right) + \frac{\vec{g}(\rho_p - \rho)}{\rho_p} + \vec{F} \tag{2-27}$$

where $\vec{u}$ is the fluid velocity, $\vec{u}_p$ is the particle velocity, ρ_p is the particle density, ρ is the fluid density, $\frac{\vec{g}(\rho_p-\rho)}{\rho_p}$ is the gravitational force, $\vec{F}$ is an additional acceleration (force/unit particle mass) term which in this study is zero, and $F_D\left(\vec{u} - \vec{u}_p\right)$ is the drag force per unit particle mass and is computed from following equation,

$$F_D = \frac{18\mu}{\rho_p d_p^2} C_D \frac{Re}{24} \tag{2-28}$$

where μ is the dynamic viscosity of fluid, d_p is the particle diameter, and Re is the relative Reynolds number defined as follows.

$$Re \equiv \frac{\rho_p d_p |\vec{u} - \vec{u}_p|}{\mu} \tag{2-29}$$

The drag coefficient (C_D) is obtained from the following equation,

$$C_D = a_1 + \frac{a_2}{Re} + \frac{a_3}{Re^2} \tag{2-30}$$

where a_1, a_2, and a_3 are constants which apply to spherical smooth particles for a wide range of Re given by Morsi and Alexander [33].

2.2.2 Particle Heat and Mass Transfer

A multicomponent model is employed as suspension droplets assumed to be a mixture of two species i.e. ethanol and YSZ. The energy equation of the multicomponent particle is calculated as [32],

$$m_p c_p \frac{dT_p}{dt} = hA_p\left(T_\infty - T_p\right) + \sum_i \frac{dm_i}{dt}\left(h_{vap,i}\right) \tag{2-33}$$

where, m_p is the particle mass, c_p is the particle specific heat, A_p is the particle surface area, T_p is the particle temperature, T_∞ is the continuous phase (plasma jet in this study) temperature, $h_{vap,i}$ is the latent heat of component i, and h is the convective heat transfer coefficient which is obtained from the correlation given by Ranz and Marshall [34], [35],

$$Nu = \frac{hd_p}{k_\infty} = \frac{\ln(1+B_{m,i})}{B_{m,i}}\left(2.0 + 0.6Re_d^{1/2}Pr^{1/3}\right) \tag{2-34}$$

where d_p is the particle diameter (m), k_∞ is the thermal conductivity of the continuous phase (W/m-K), Re_d is the Reynolds number, Pr is the Prandtl number of the continuous phase $\left(c_p\mu/k_\infty\right)$, and $B_{m,i}$ is the Spalding mass number for species i and is given by,

$$B_{m,i} = \frac{Y_{i,S}-Y_{i,\infty}}{1-Y_{i,S}} \tag{2-35}$$

where, $Y_{i,S}$ is the vapor mass fraction at the surface and $Y_{i,\infty}$ is the vapor mass fraction in the bulk gas.

The evaporation of the multicomponent is computed from the sum of the individual species' vaporization rate,

$$\frac{dm_i}{dt} = A_p k_{c,i}\rho_\infty ln\left(1 + B_{m,i}\right) \tag{2-36}$$

where ρ_∞ is the gas density (kg/m^3) and $k_{c,i}$ is the mass transfer coefficient of component i (m/s) calculated by the Sherwood number correlation [34], [35],

$$Sh_{AB} = \frac{k_{c,i}d_p}{D_{i,m}} = 2.0 + 0.6Re_d^{1/2}Sc^{1/3} \tag{2-37}$$

where $D_{i,m}$ is the diffusion coefficient of vapor in bulk (m^2/s) and Sc is the Schmidt number $\left(\mu/\rho D_{i,m}\right)$.

2.2.3 Breakup Model Theory

When the suspension droplets are injected into the plasma jet, due to the interacting with the core of the plasma plume, the droplets start to break up. At the time that the suspension viscosity is low (i.e. low Ohnesorge number), Weber number is used to classify the secondary breakup processes,

$$We = \frac{\rho V^2 D}{\sigma} \tag{2-38}$$

where, ρ is the flow field density, V is the initial relative velocity between the flow field and the droplets, D is the initial diameter of the droplet, and σ is the droplet surface tension.

One of the classifications based on the Weber number done by Pilch and Erdman [36] is shown in Figure 2.6. Based on this classification, when the Weber number is less than 12, breakup does not occur and there is only some droplet deformation.

$12 \leq We \leq 100$ → Bag Breakup

$100 \leq We \leq 350$ → Stripping Breakup

$350 \leq We$ → Catastrophic Breakup

Considering the above classification, the breakup regime of suspension droplets in the SPS process is recognized as catastrophic breakup. For high Weber number conditions, the Kelvin-Helmholtz Rayleigh-Taylor breakup model is suggested.

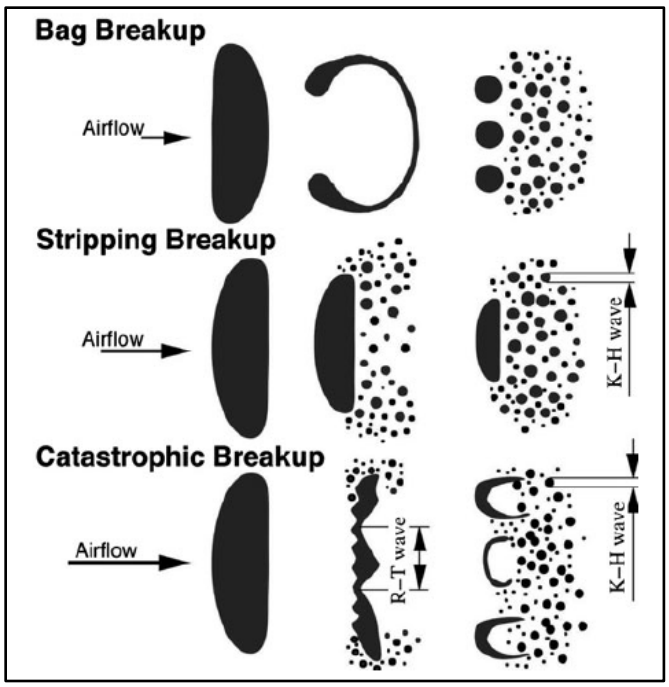

Figure 2.6- Breakup regimes based on Weber number [37]

The KHRT breakup model combines the Kelvin-Helmholtz waves obtained from the aerodynamic forces with the Rayleigh-Taylor wave instabilities on the droplet surface. To model the liquid core near the nozzle region, a theory given by Levich is used to calculate the liquid core length [32],

$$L = C_L d_0 \sqrt{\frac{\rho_l}{\rho_g}} \tag{2-39}$$

where C_L is the Levich constant and d_0 is a reference nozzle diameter. Figure 2.7 shows the length of the liquid core. Inside the liquid core region, only aerodynamic breakup is considered (Kelvin-Helmholtz wave growth) and the child droplets are shed from this core. When the droplets are ejected to the free stream, the Rayleigh-Taylor instability becomes dominant. Therefore, inside the liquid core region, the Wave model is used to compute the breakup while outside this region, KH and RT effects are both considered in breakup calculation.

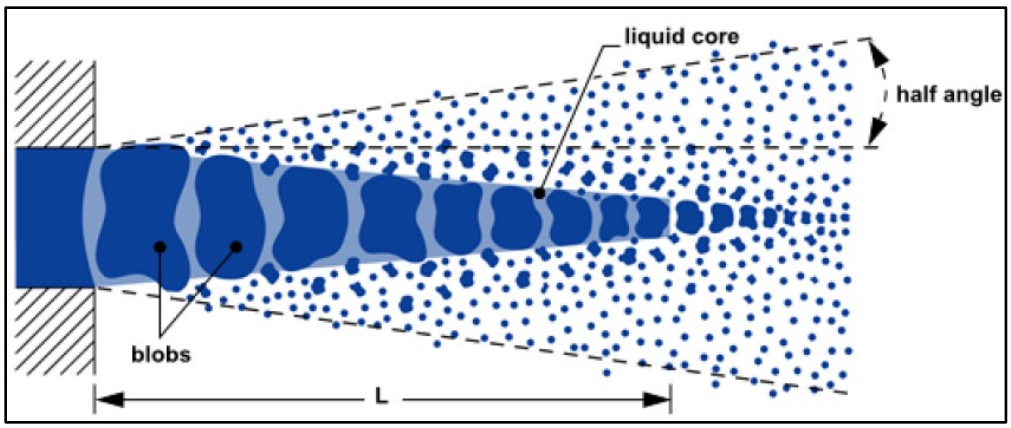

Figure 2.7- Liquid core length approximation [32]

Wave Breakup Model

In Wave model, the breakup time and the resulting droplet size are computed from the Kelvin-Helmholtz instability derived from the jet stability analysis. To determine the dispersion relation, the linearized equations for the liquid hydrodynamics are solved considering the wave solutions [32],

$$\emptyset_1 = C_1 I_0(kr) e^{ikz+\omega t} \tag{2-40}$$

$$\psi_1 = C_2 I_1(Lr) e^{ikz+\omega t} \tag{2-41}$$

where $\emptyset_1$ is the velocity potential, ψ_1 is the stream function, C_1 and C_2 are the integration constants, I_0 and I_1 are the modified Bessel functions of the first kind, $L^2 = k^2 + \omega/\vartheta_1$, and ϑ_1 is the liquid kinetic viscosity.

In this model, the radius of the newly formed droplet is calculated corresponding to the wavelength of the fastest-growing unstable surface wave on the parent droplet,

$$r = B_0 \Lambda \tag{2-42}$$

where B_0 is the model constant (0.61). The rate of the droplet radius is computed from,

$$\frac{da}{dt} = -\frac{(a-r)}{\tau}, \qquad r \leq a \tag{2-43}$$

here τ is the breakup time and is obtained from,

$$\tau = \frac{3.726 B_1 a}{\Lambda\Omega} \tag{2-44}$$

where B_1 is the breakup time constant (1.73). Λ and Ω are given by following equations,

$$\frac{\Lambda}{a} = 9.02 \frac{(1+0.45Oh^{0.5})[1+0.4Ta^{0.7}]}{(1+0.8We_2^{1.67})^{0.67}} \tag{2-45}$$

$$\Omega\left(\frac{\rho_1 a^3}{\sigma}\right) = \frac{(0.34+0.38We_2^{1.5})}{(1+Oh)(1+1.4Ta^{0.6})} \tag{2-46}$$

where Oh is the Ohnesorge number ($Oh = \frac{\sqrt{We_1}}{Re_1}$) and Ta is the Taylor number ($Ta = Oh\sqrt{We_2}$). We_1 and We_2 are the liquid and gas Weber number respectively.

In the Wave breakup model, a new parcel with the radius obtained from equation (2-42) is created when the shed mass becomes equal to 5 % of the initial mass. Except for radius and velocity, the new parcel's properties such as temperature, material, and position are the same as the parent parcel's.

Rayleigh-Taylor Breakup

The frequency of the fastest growing wave in Rayleigh-Taylor model is given by [32],

$$\Omega_{RT} = \sqrt{\frac{2\left(-g_t(\rho_p-\rho_g)\right)^{3/2}}{3\sqrt{3\sigma}(\rho_p+\rho_g)}} \tag{2-47}$$

where g_t is the droplet acceleration in the direction of the droplet travel. The corresponding wave number is calculated from,

$$\mathrm{K}_{RT} = \sqrt{\frac{-g_t(\rho_p-\rho_g)}{3\sigma}} \tag{2-48}$$

The breakup time (τ_{RT}) is obtained from,

$$\tau_{RT} = \frac{C_\tau}{\Omega_{RT}} \tag{2-49}$$

Breakup happens when the RT waves have been grown in the larger time than the breakup time.

Until the predicted wave length $(2\pi C_{RT}/\mathrm{K}_{RT})$ is smaller than the local droplet diameter, the wave growth is continued to track. The smaller child droplet radius is obtained from,

$$r_c = \frac{\pi C_{RT}}{\mathrm{K}_{RT}} \tag{2-50}$$

2.3 Geometry and Computational Domain

The 3MB Metco gun with the total length of 32.15 mm and diameter of 5.5 mm in the straight part of the gun is used in this study (Figure 2.8). The length of the gun in the straight part is 22.5 mm. The cathode and the inlet with an angle of 45° which causes swirling flow in the plasma jet are considered in the simulation. Geometry and computational domain of the study employed in the simulations are shown in Figure 2.9. The inlet diameter is 3.6 mm. The outlet domain is an incomplete cone with initial and final diameters of 60 and 100 mm, respectively, and a length of 140 mm (see Figure 2.10).

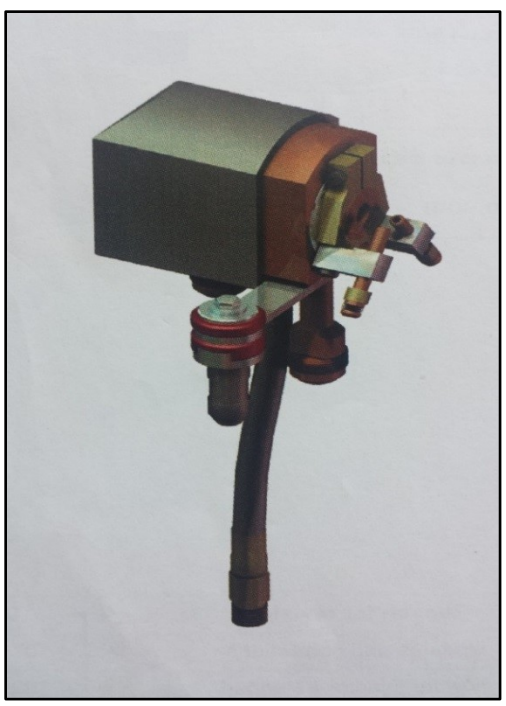

Figure 2.8- 3MB plasma spray gun [38]

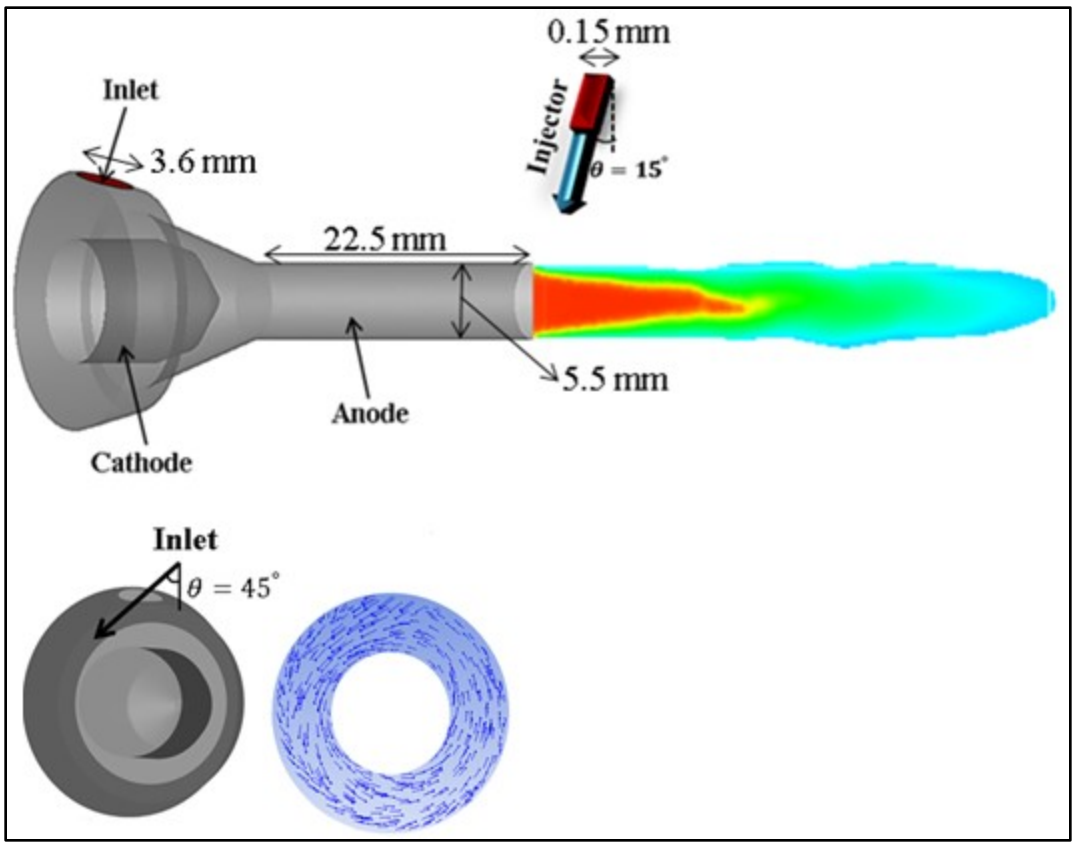

Figure 2.9- Geometry of domain of study and direction of inlet flow

The computational domain contains about 800,000 cells which are the mixed of tetrahedral and hexahedral volume meshes. The cell sizes are locally refined in the plasma core area inside and outside the gun to capture the large plasma temperature and velocity gradients. Figures 2.10 and 2.11 illustrate the mesh sizes used in the domain of this study.

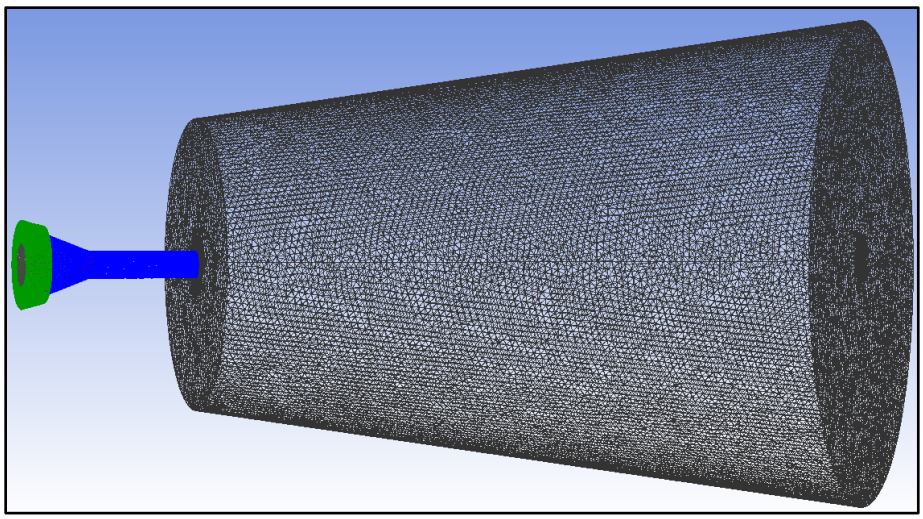

Figure 2.10- Computational mesh of the domain of study

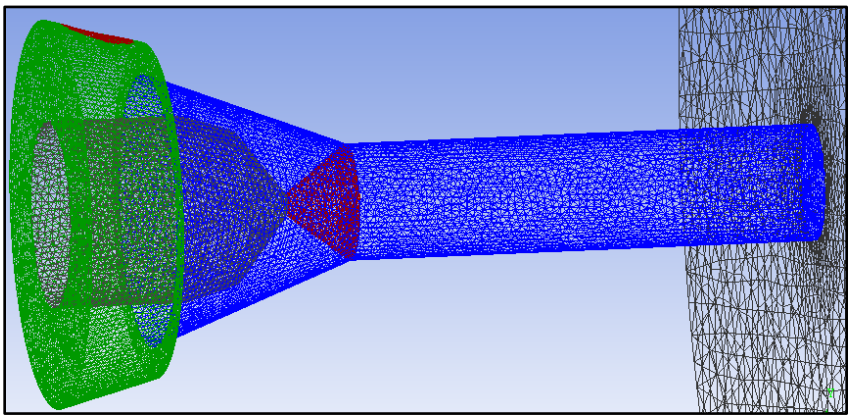

Figure 2.11- Finer mesh inside the plasma gun

The following assumptions are considered in this study:

- The flow is time-dependent.
- Physical and chemical properties of plasma gases (mixture of argon and hydrogen) which are temperature-dependent are added to the model.
- The plasma is in local thermodynamic equilibrium and optically thin.

2.4 Operating and Boundary Conditions

The plasma torch operating condition is shown in Table 2.1.

Table 2.1- Operating condition for plasma spraying simulation

Operating Condition	Magnitude
Current Input (A)	600
Average Voltage (V)	51
Thermal Efficiency (%)	58
Ar/H_2 gas flow rate (slm)	47.5/2.5

Mass flow rate with turbulent intensity and hydraulic diameter as the turbulence model are used for the inlet boundary. The turbulence intensity is calculated from Eq. (2-51) [39],

$$T_i = 0.16(Re_{HD})^{-0.125} \tag{2-51}$$

where, Re_{HD} is the Reynolds number calculated for the gas flowing through the respective inlet on the basis of the hydraulic diameter as the characteristic length.

The anode temperature is fixed at 300 K due to using the water cooling technique around it. For the outlet boundaries, pressure outlet condition is used. Radiation loss introduced by using a sink term in the enthalpy equation is shown in Figure 2.12.

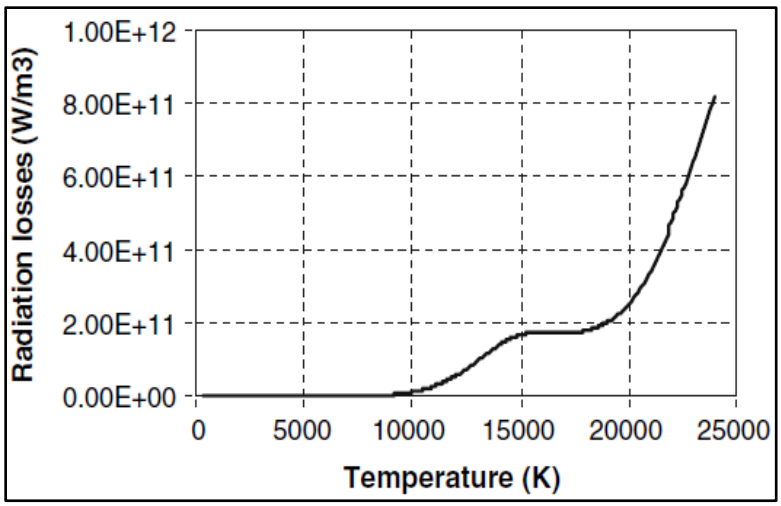

Figure 2.12- Radiation losses versus temperature for argon/hydrogen mixture [27]

Figure 2.13(a) illustrates the typical arc voltage fluctuations recorded on the plasma torch during spraying. In this study, a Fourier series is used to create a periodic function (Figure 2.13(b)) with similar characteristics,

$$E(t) = a_0 + \sum_{n=1}^{8} a_n cos(n\omega t) + \sum_{m=1}^{8} b_m sin(m\omega t) \quad (2\text{-}52)$$

where, $E(t)$ is the arc voltage, a_0 is the average voltage, $a_1, \ldots, a_n$, $b_1, \ldots, b_n$, and ω are the function coefficients (Table 2.2). Arc voltage oscillates between 42 and 63 V with a fundamental frequency of 4167 Hz.

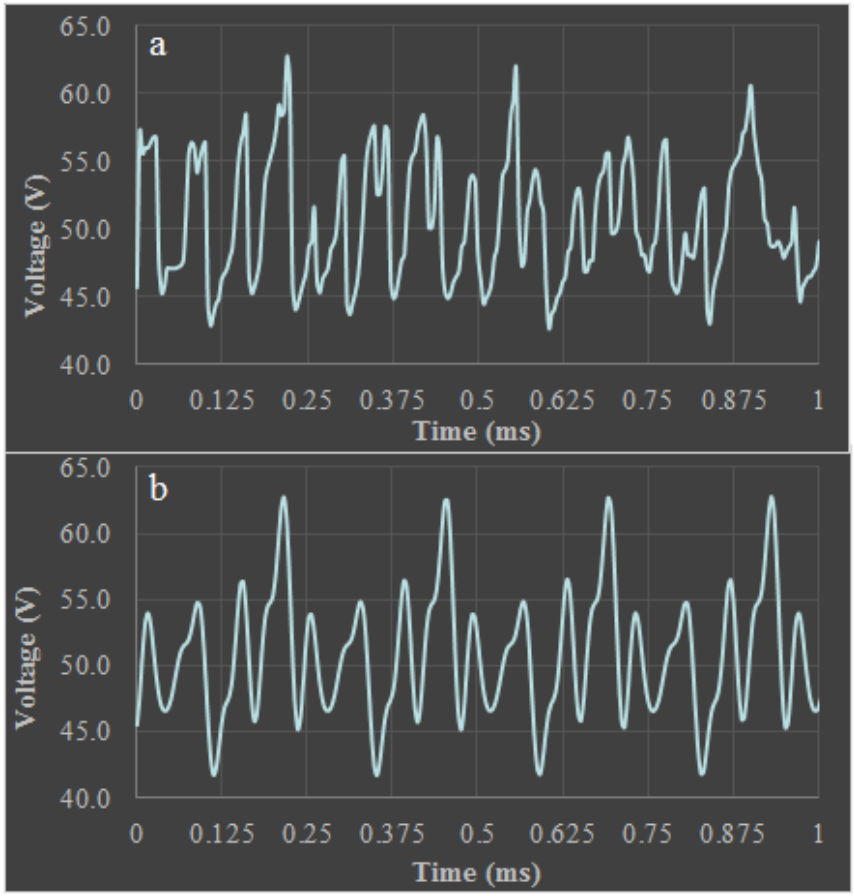

Figure 2.13- Arc voltage fluctuations- Ar_H_2-(a) typical, (b) modeled with Fourier series

Table 2.2- Coefficients of modeled voltage fluctuations function

a_0	a_1	a_2	a_3	a_4	a_5	a_6	a_7	a_8
50.84	2.1280	-1.15580	1.29060	-3.9420	-0.62300	-1.13420	-1.79220	-0.106340
w	b_1	b_2	b_3	b_4	b_5	b_6	b_7	b_8
2.63e+04	-1.79520	-2.350	-1.51720	1.0490	1.11620	0.58580	-0.194180	1.5320

Plasma Heat Generation

In the current research, in order to model the plasma jet, at first in the steady state, Joule effect is taken into account on the cone volume (V_1) and the cylinder heating zone inside the torch (V_2) to find the mean value of the length (L_m) corresponding to the mean power (Figure 2.14). In this case, arc voltage oscillations which cause axial fluctuations are not considered in the simulation.

However, there are still azimuthal fluctuations due to the plasma swirling flow. Therefore, the steady case has been renamed to the quasi-steady case.

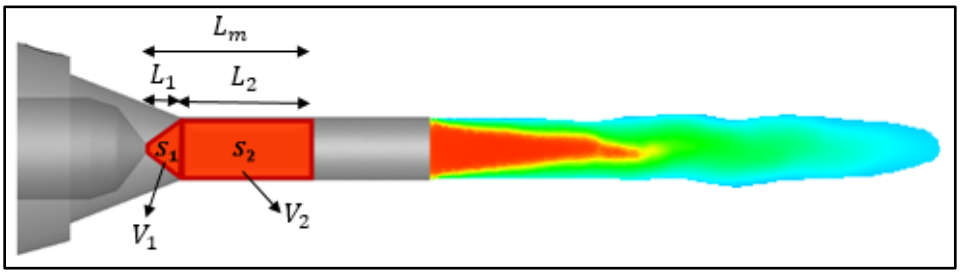

Figure 2.14- Plasma torch with the heating zones V_1 and V_2 (quasi-steady)

The obtained results from the quasi-steady case are validated by comparing the thermal efficiency from equation (2-53) [27] and the experimental thermal efficiency,

$$\eta = 1 - \left(\frac{H_{conv}+H_{rad}}{P_m}\right) \tag{2-53}$$

where, H_{conv} and H_{rad} are the convection losses and the radiation losses inside the torch respectively. H_{conv} is obtained from the numerical results and H_{rad} is calculated from Fig. 2.12. After several try-and-error calculations, the average length value is obtained as a length of 16 mm from the cathode tip.

The quasi-steady case results are used to model the unsteady plasma jet. In unsteady state, the voltage fluctuation is used as input data (Fig. 2.13) and $L_2(t)$ is a function of voltage fluctuations (Figure 2.15),

$$L_2(t) = aE(t) + b \tag{2-54}$$

where a and b are the constants obtained from $L_{\min}$ and $L_{\max}$ corresponding to $E_{\min}$ and $E_{\max}$ respectively. $E(t)$ is the arc voltage fluctuation derived from Fig 2.13.

To generate the plasma heat and voltage fluctuations, volumetric heat sources are introduced inside the plasma torch and added to the energy equation.

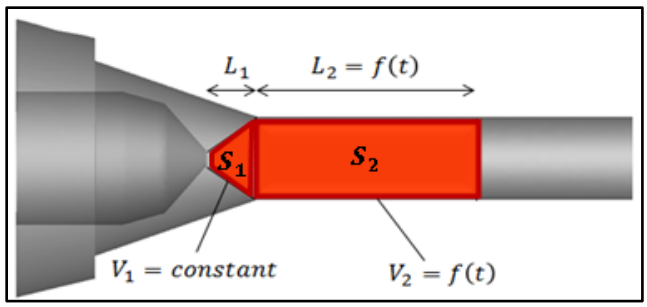

Figure 2.15- Plasma torch with the heating zones V_1 and $V_2(t)$

As shown in Figure 2.15, the volume 1 (V_1) and $L_1 = 3$ mm are always constant due to the connecting with the torch geometry. However, the volume 2 (V_2) and L_2 are time-dependent as defined in the following equations [27],

$$\begin{cases} P_1 = \frac{P_m}{L_m} L_1 & \rightarrow \quad S_{\mathrm{h1}} = \frac{P_1}{V_1} = C_1 \\ P_2(t) = \frac{P_m}{L_m} L_2(t) & \rightarrow \quad S_{\mathrm{h2}} = \frac{P_2(t)}{V_2(t)} = C_2 \end{cases} \tag{2-55}$$

$$P = EI \tag{2-56}$$

where L_m is the average length corresponding to the mean power (P_m), P_1 and S_{h1} are the power and the volumetric heat source of V_1 respectively, P_2 and S_{h2} are the power and the volumetric heat source of V_2 respectively.

SPS Modeling

In this study, suspension injection in the form of a continuous jet is substituted with a chain of fragmented droplets with a uniform size of 150 µm equal to the injector diameter and velocity of 24.4 m/s are injected radially with a reverse angle of $\theta = 15^{\circ}$ with respect to the normal plane to the plasma jet (Figure 2.16). Droplets are injected every 1 µs with the suspension mass flow rate of 22 g/min. The thermo-physical properties of materials used in this study are given in Table 2.3.

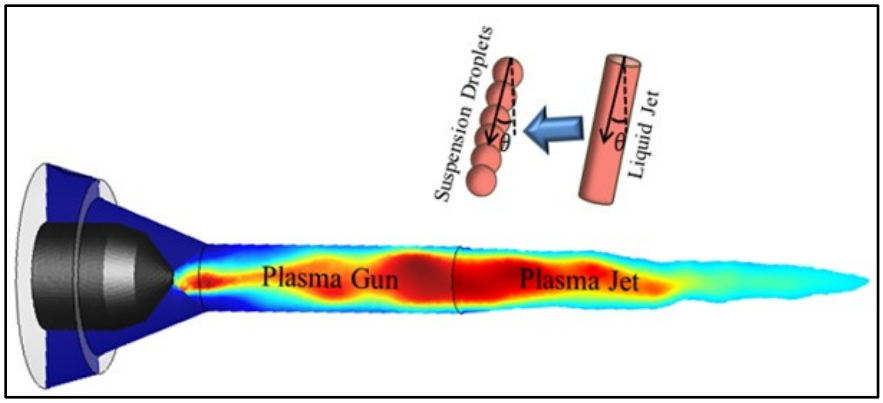

Figure 2.16- Schematic of injected droplets into the plasma jet

Table 2.3- Material thermos-physical properties [21], [39]

Property	Ethanol	Zirconia
Density $(\mathrm{kg/m^3})$	790	5890
Viscosity $(\mathrm{kg/m.s})$	0.0012	0.038285
Melting Latent Heat $(\mathrm{J/kg})$	…	7.06×10^5
Boiling Latent Heat $(\mathrm{J/kg})$	855237	9×10^6
Melting Point (K)	…	2988
Boiling Point (K)	351	5273
Surface Tension $(\mathrm{N/m})$	0.022348	1.5

3 Results and Discussion

Overview

In this chapter, the numerical results for the effect of the continuous phase considering the arc voltage fluctuations and azimuthal fluctuations on the disperse phase will be presented. In addition, effects of changing operation parameters like suspension feed rate and different distances from the gun exit will be discussed. Furthermore, to see the rate of azimuthal and axial fluctuations effects on SPS properties, a case with only the azimuthal fluctuations is created and compared to the case of this study.

3.1 Continuous Phase

In order to simulate SPS process, the first step is to model the plasma jet. In the current study, plasma heat generation is modeled by introducing energy sources inside the plasma torch and the only validation criterion is the thermal efficiency parameter which is adjusted by the plasma column length inside the torch. The results of the quasi-steady and transient configurations are shown and explained in the following sections.

3.1.1 Quasi- Steady Plasma Flow

In the steady state, the mean heating zone length (L_m) is adjusted according to the mean power and thermal efficiency parameter. In this case which is called quasi-steady state, the plasma jet oscillations are limited to the azimuthal fluctuations due to the plasma gas swirling flow. Considering the thermal efficiency value (58%) acquired from experiments and the value of mean power (30.6 kW), L_2 and L_m are obtained as 13 and 16 mm, respectively. The resulting plasma gas temperature and velocity fields are illustrated in Figures 3.1(a) and 3.1(b), respectively. Dissymmetry gas flow field shown in Figure 3.1 is the result of the azimuthal fluctuations.

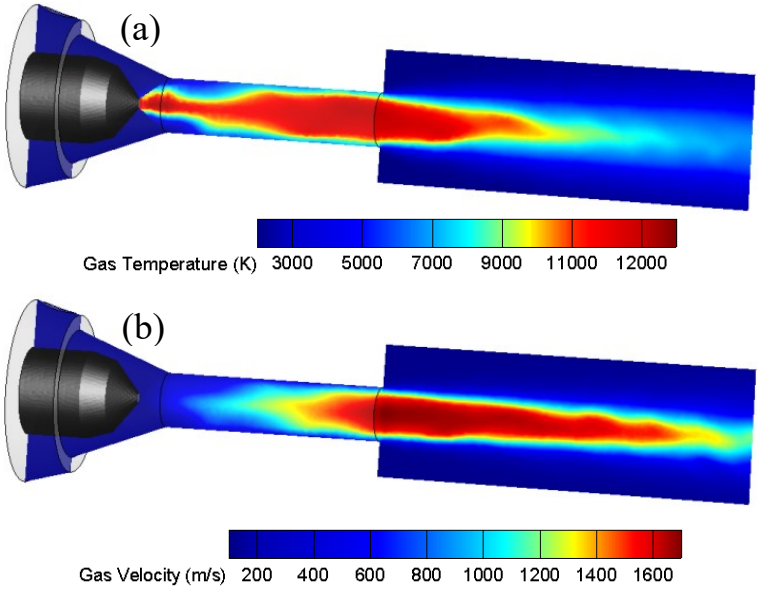

Figure 3.1- Plasma gas- (a) temperature and (b) velocity contours

3.1.2 Mesh Sensitivity Analysis

One of the key factors in the numerical modeling is the grid size sensitivity analysis. In the current study, this test is applied on the continuous phase in quasi-steady state. A coarse grid size with a total of 723297 elements and a fine grid size with a total number of 1639834 elements, which is more than two times the number of elements than with the coarse mesh, are chosen. Figure 3.2 shows the results of the gas temperature and velocity with two different mesh sizes. As shown in Figure 3.2, there is no significant difference in the results obtained from the two mesh sizes. The largest difference is less than 4%. Therefore, in order to reduce the computational cost and time of the modelling, the course mesh size is used in this study.

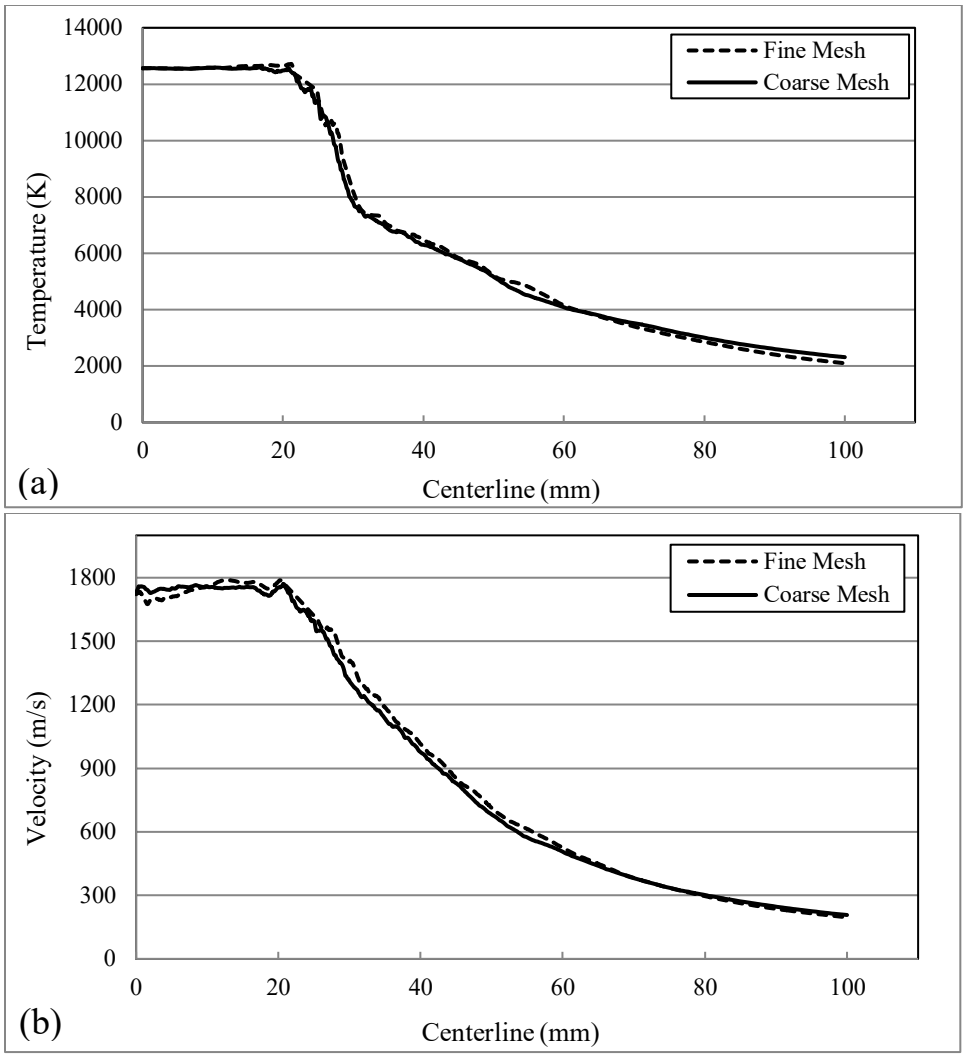

Figure 3.2- Effect of the grid size on plasma gas- (a) temperature and (b) velocity

3.1.3 Transient Plasma Flow

The focus of this study is to investigate the effect of plasma jet oscillations on the in-flight particle properties. Considering the voltage fluctuations, the power varies between 25.2 and 37.8 kW. Using the mean value calculated in the quasi-steady case and the power variation in the transient case, L_{min} and L_{max} which are the minimum and maximum length from the cathode tip are obtained as 13.1 and 19.7 mm, respectively. To capture the voltage fluctuations with a period of 0.24 ms, the selected time step to model the oscillating plasma jet is 0.01 ms. However, in

order to save the hard disk space, the writing time step for storing data is 32 times of the plasma gas flow time step, or in other word, it is equal to $1.33 \times voltage\ fluctuation\ period$. Figure 3.3(a) shows the saved data and Figure 3.3(b) illustrates the voltage fluctuations used in this study and six points which show the saved data from Figure 3.3(a).

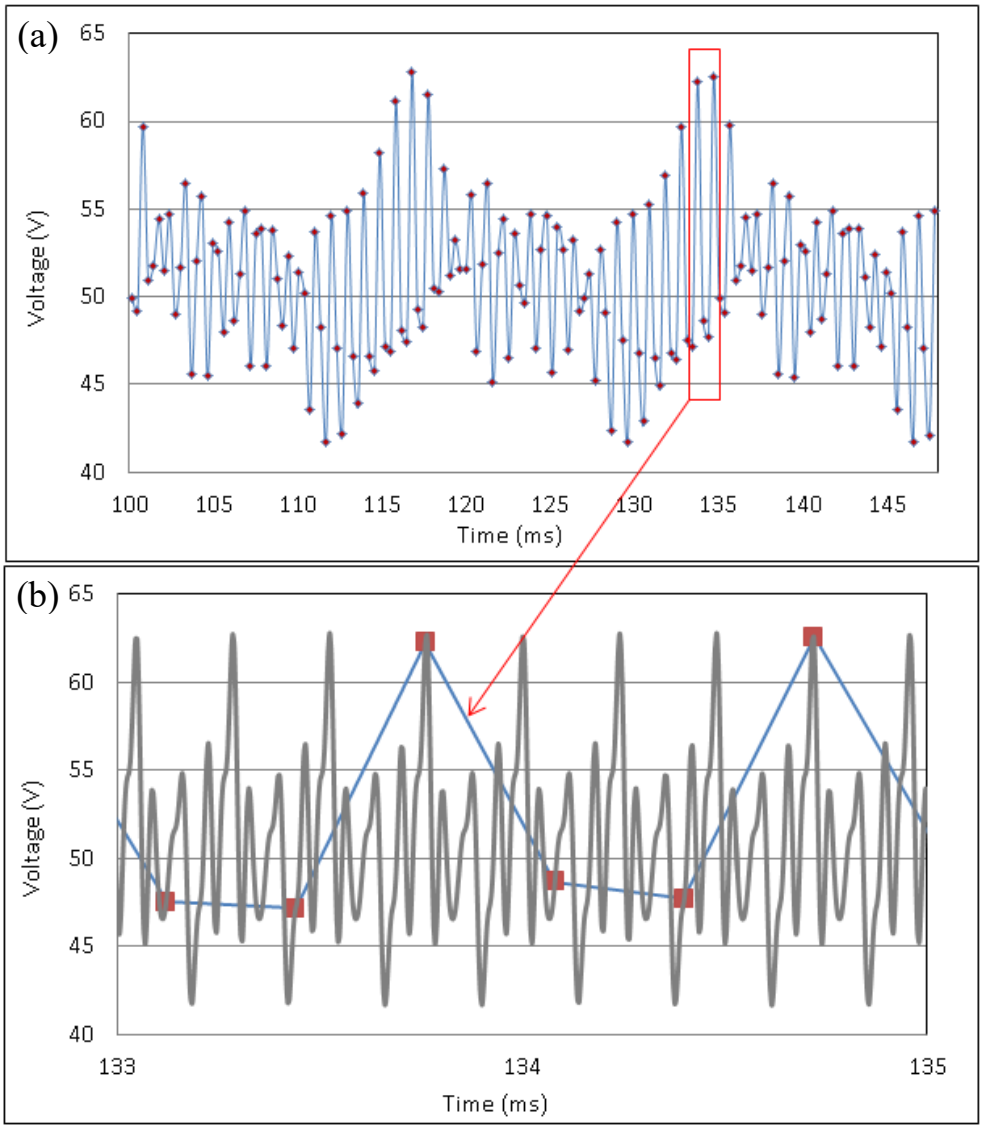

Figure 3.3- (a) Arc voltage of the saved data and (b) Used arc voltage fluctuations

In order to see the transient configuration results, the plasma gas temperature and velocity distributions of three different moments regarding to their arc voltage are shown in Figures 3.4

and 3.5, respectively. To see the length of the plasma jet at these moments, an isosurface temperature of 11000 K and an isosurface velocity of 1600 m/s are selected, respectively.

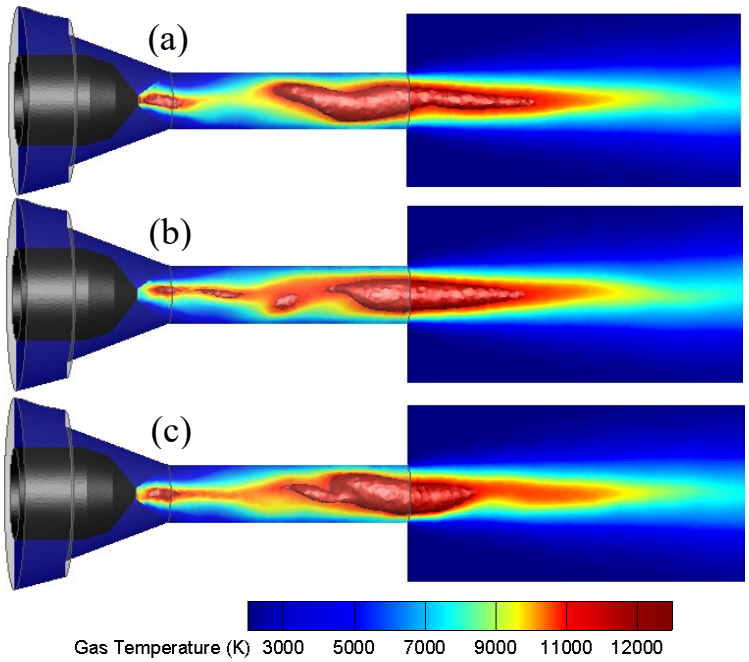

Figure 3.4- Plasma gas temperature with a current input of 600A and arc voltage of (a) 62, (b) 50 and (c) 42 V

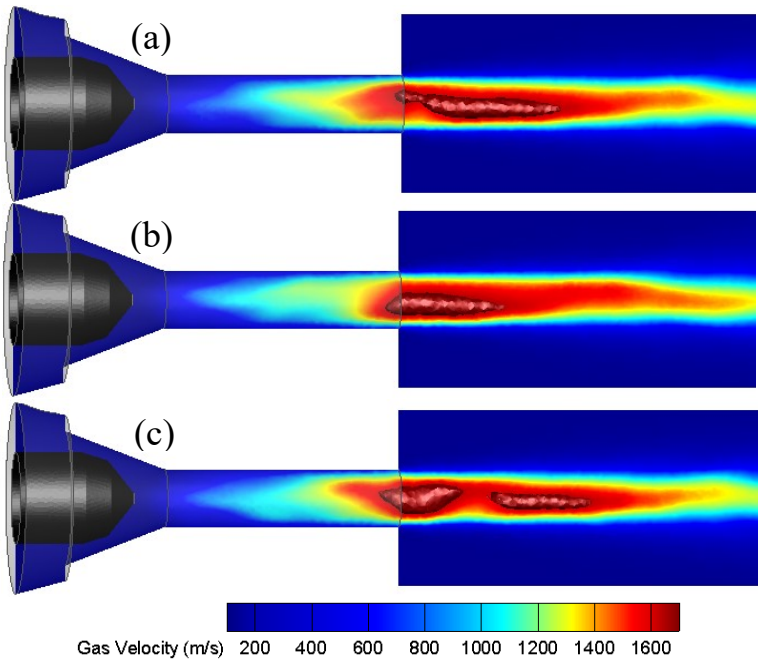

Figure 3.5- Plasma gas velocity with a current input of 600A and arc voltage of (a) 62, (b) 50 and (c) 42 V

Azimuthal fluctuations due to the plasma gas swirling having a counterclockwise rotation can be also seen in Figures 3.6 and 3.7, which show the plasma gas temperature and velocity

contours respectively in four different moments. The plane shown in Figures 3.6 and 3.7 is selected at 6 mm from the gun exit which is the location of the injection.

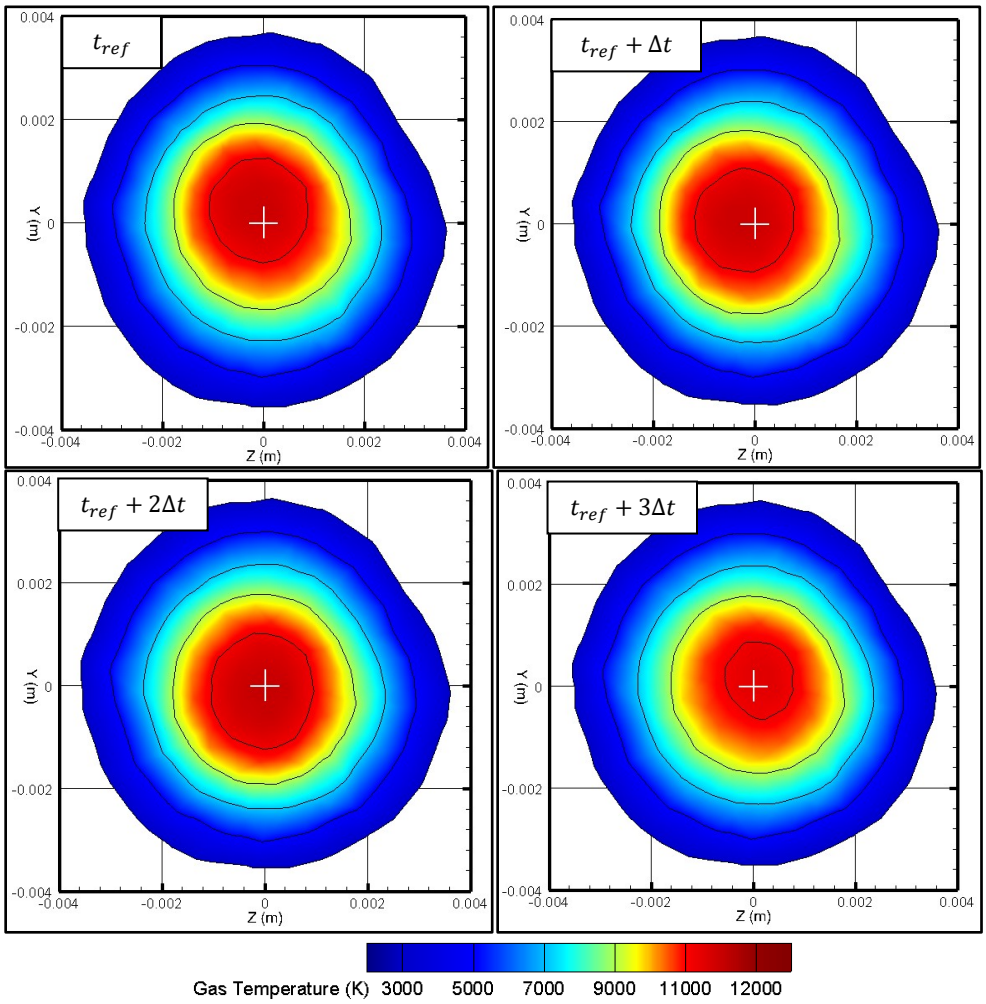

Figure 3.6- Gas plasma temperature contours at a stand-off distance of 6 mm (4 snap shots)

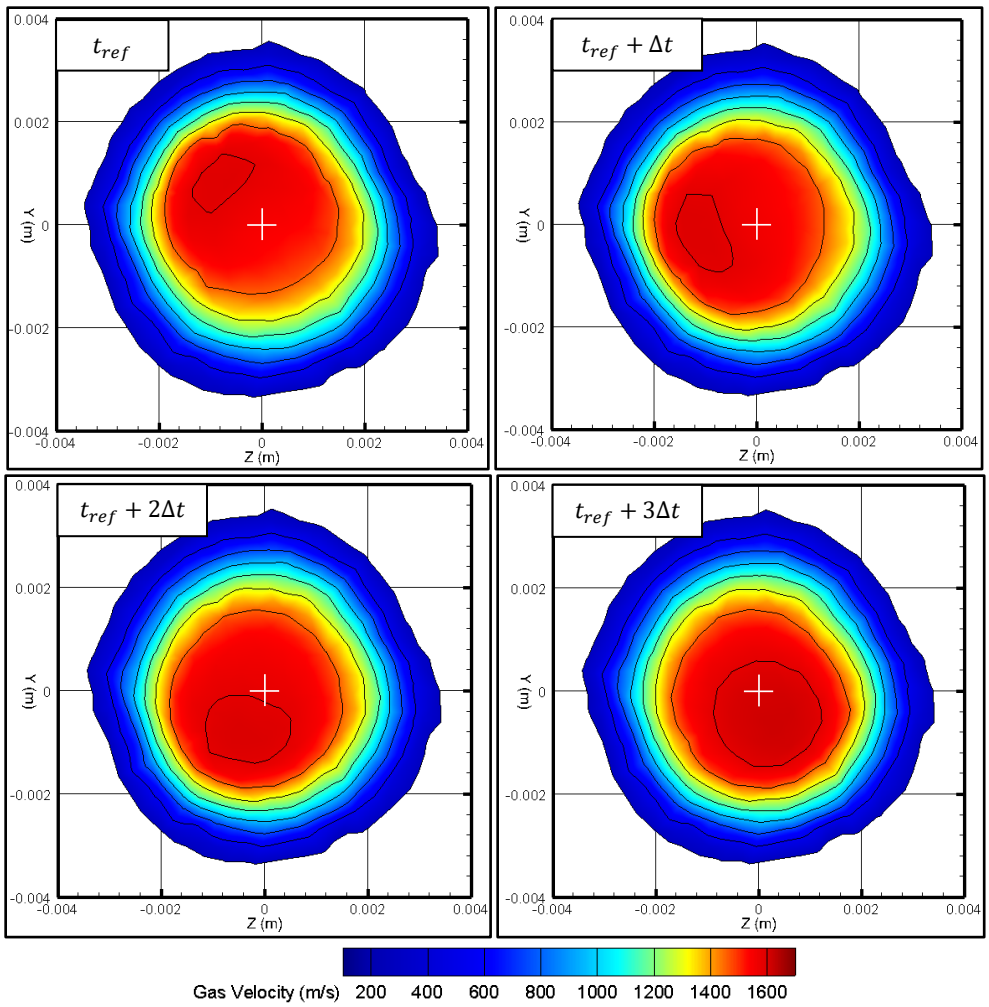

Figure 3.7- Gas plasma velocity contours at a stand-off distance of 6 mm (4 snap shots)

Figure 3.8 shows the total behavior of plasma jet due to both azimuthal and voltage fluctuations in three different moments with the isosurface temperature of 11000 K. In this figure, the streamlines are colored by plasma gas temperature and show the swirling gas flow and the arrows illustrate the rotation direction of the gas flow which is counterclockwise.

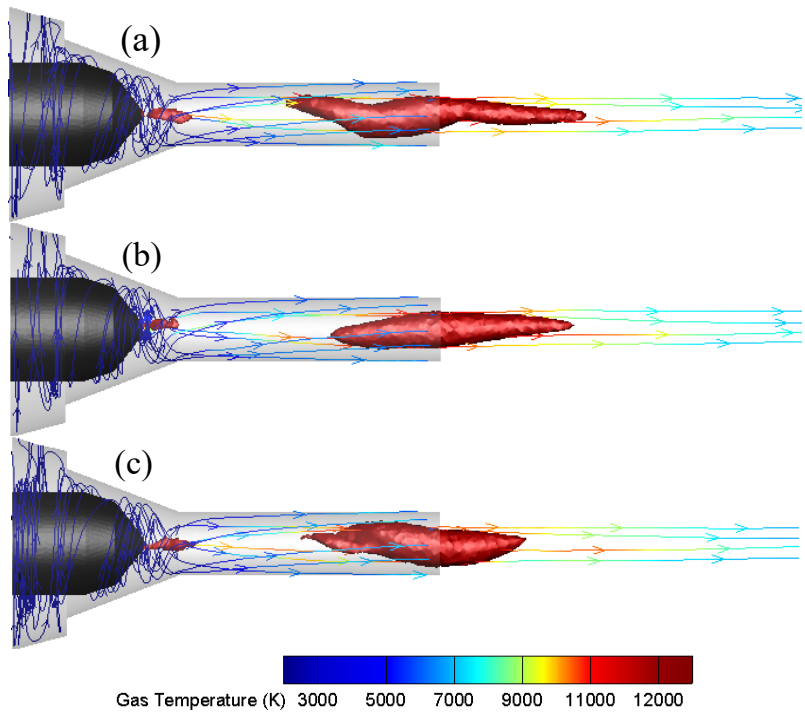

Figure 3.8- Streamlines colored by plasma gas temperature and isosurface temperature of 11000 K with current input of 600 A and arc voltages of (a) 62, (b) 51 and (c) 42 V

3.2 Discrete Phase

For the verification of the multicomponent heat transfer, a theoretical case with a 25 micron droplet situated at the center of the nozzle exit, is created. In order to simplify the model in this case, the droplet break up is not considered. Figure 3.9 illustrates how the droplet's temperature evolves as a function of time while the droplet is moving inside the plasma. Figure 3.9 (a) shows that the particle temperature increases to nearly 4500 K after ethanol evaporates and then the temperature decreases when it moves along the centerline. In Figure 3.9(a), the first plateau shows the time needed to evaporate ethanol and Figure 3.9(b) represents the time which zirconia particles melt.

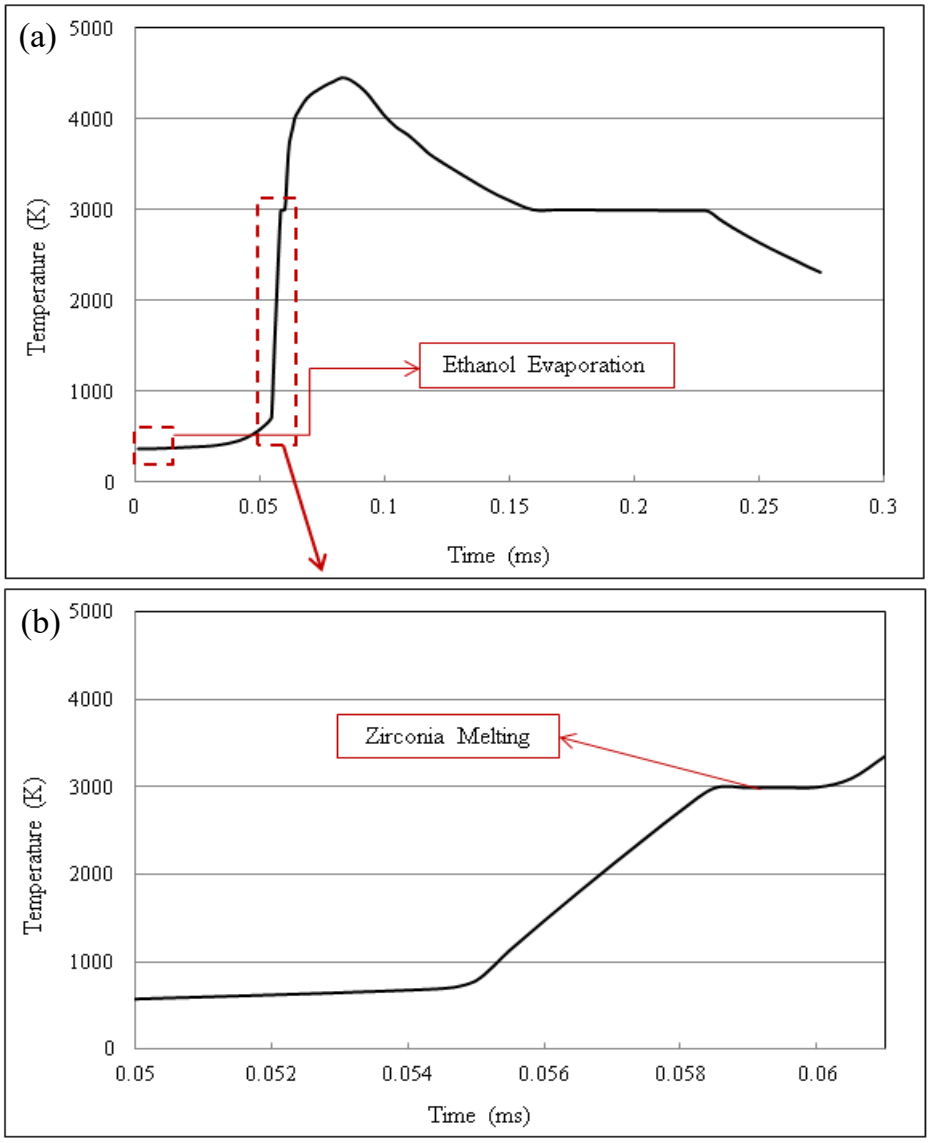

Figure 3.9- Evolution of the temperature of a 25 μm particle as a function of time

In the next step, results of the oscillating plasma jet are used to initialize the model in the case of suspension injection. Figure 3.10 illustrates the particle temperature distribution after their interaction with the oscillating plasma jet. In this figure, an isosurface of temperature equal to 10400 K in three different moments is introduced to show the plasma jet oscillations. Three moments (a), (b) and (c) illustrated in Figure 3.10 have a constant current of 600 A and different voltages of 62, 56, and 46 V, respectively.

It can be observed that fine particles located near the plasma torch centerline have gained higher temperature compared to the other particles with larger size due to their weak penetration. Another important result which can be concluded from Figures 3.10, 3.11 and 3.12 shows that in any given distance from the gun exit, the particle temperatures and velocities vary in time due to the oscillations.

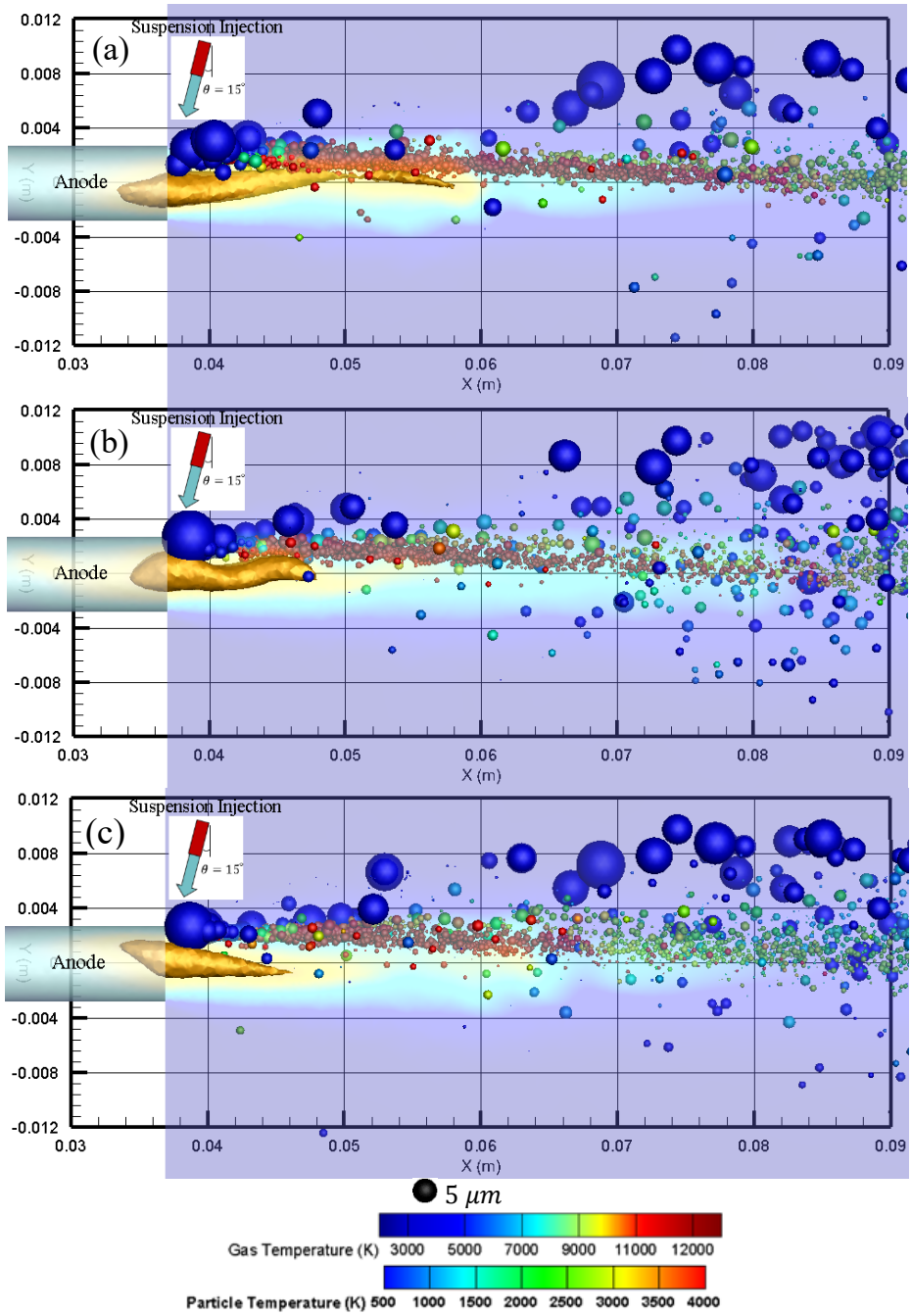

Figure 3.10- Particle temperature and plasma gas temperature with a current input of 600 A and arc voltages of (a) 62, (b) 56 and (c) 46 V

In order to better understand the effects of the arc fluctuations on particle properties, two different distances (40 and 60 mm) from the gun exit are investigated. Figure 3.11 shows the plasma and particle temperatures in the three moments shown in Figure 3.10 at 40 mm (a_1, a_2, and a_3) and 60 mm (b_1, b_2, and b_3) from the gun exit. Figure 3.12 represents the plasma and particles velocity in the same moments.

It can be concluded that the majority of the particles are located in the left side of the cross sections shown in Figures 3.11 and 3.12 due to the plasma jet counterclockwise rotation. Furthermore, it can be seen that the particle temperature, velocity, and position from the centerline are also changed in presence of the plasma jet fluctuations. Moreover, a wide range of particle size is observed as the result of the plasma oscillations. Consequently, particles with lower temperature and larger diameter might cause imperfections in SPS coatings.

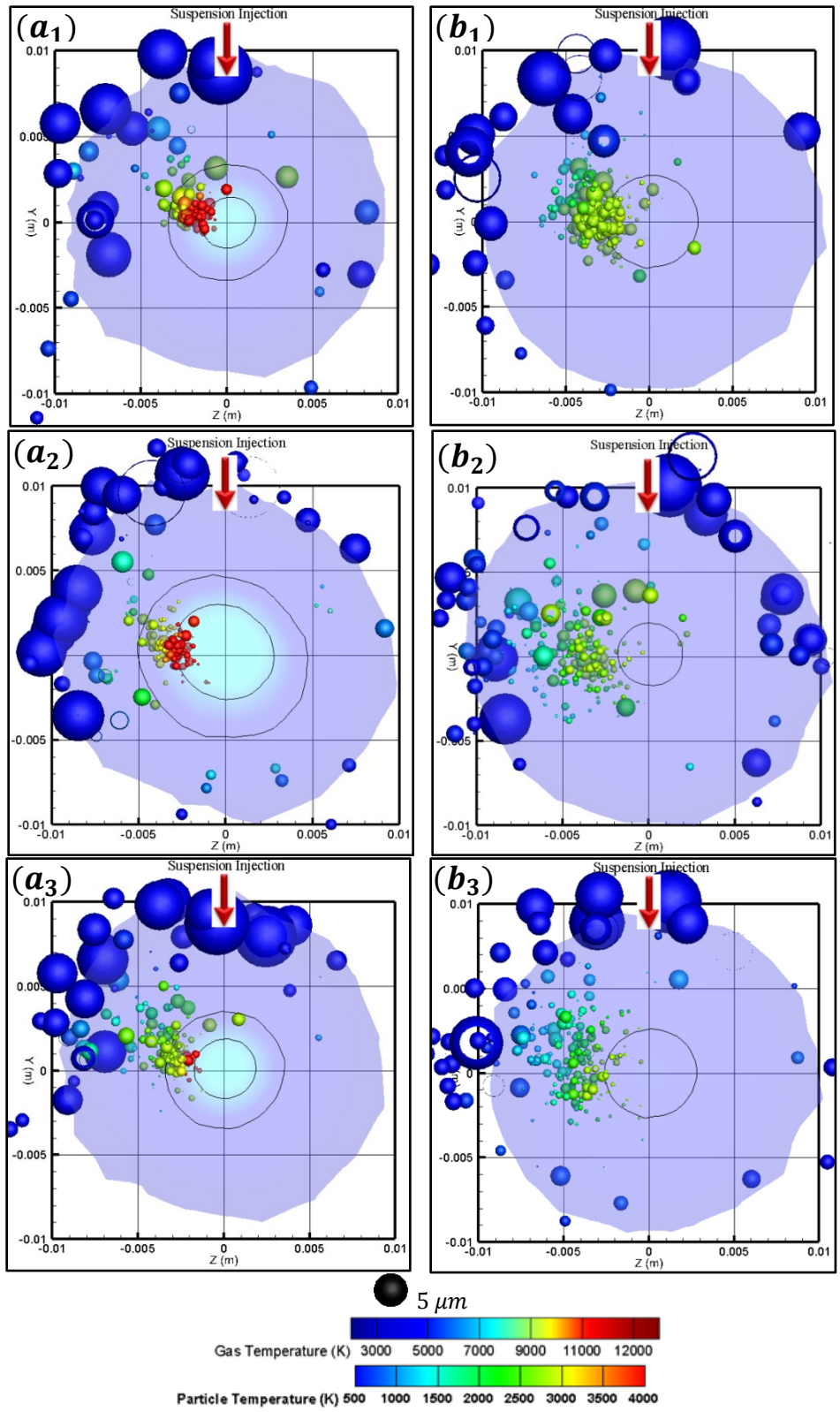

Figure 3.11- Particle temperature and plasma gas temperature at 40 mm from the gun exit with arc voltages of (a_1) 62, (a_2) 56, and (a_3) 46 V and 60 mm from the gun exit with arc voltages of (b_1) 62, (b_2) 56, and (b_3) 46 V

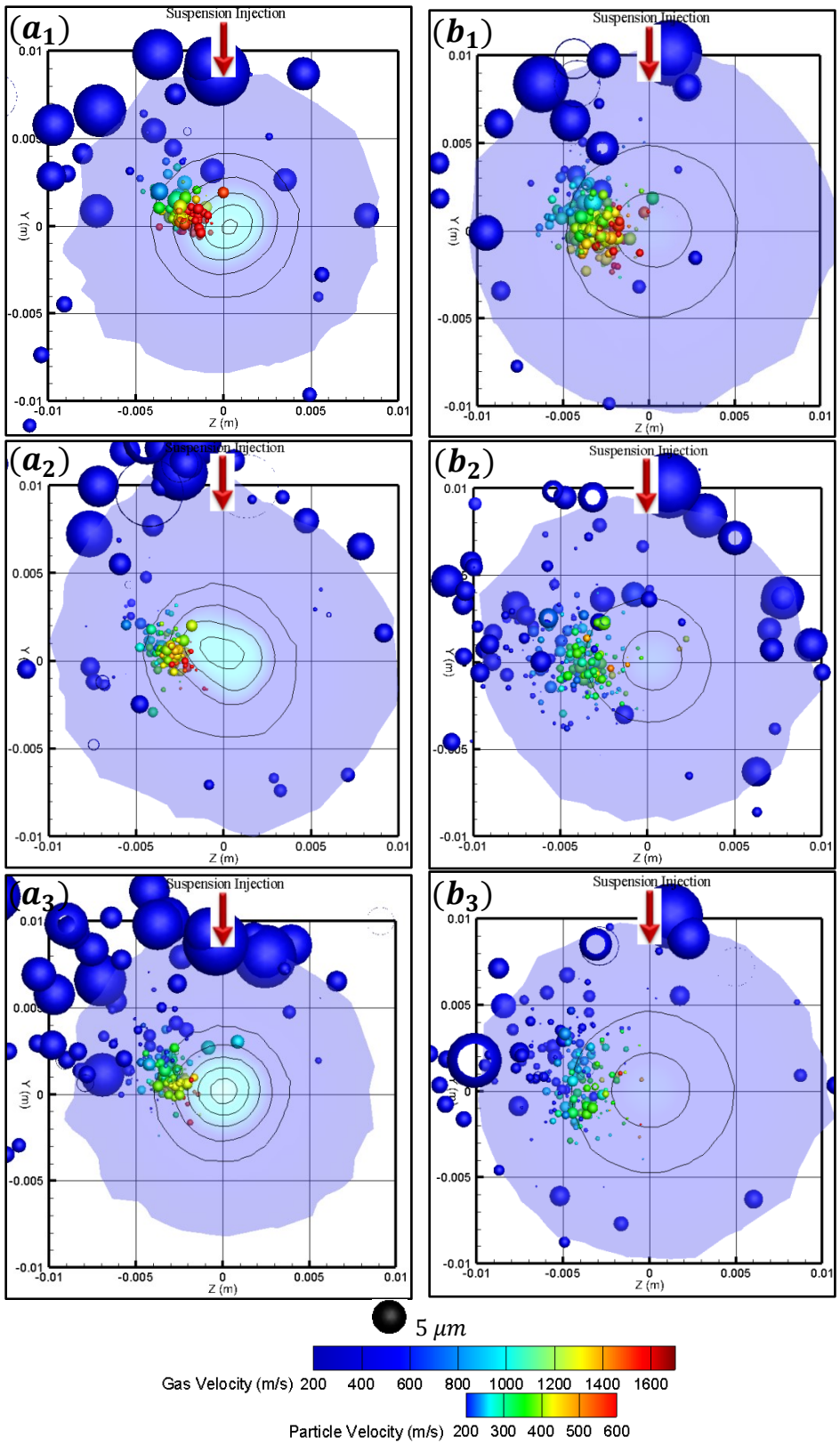

Figure 3.12- Particle velocity and plasma gas velocity at 40 mm from the gun exit with arc voltages of (a_1) 62, (a_2) 56, and (a_3) 46 V and 60 mm from the gun exit with arc voltages of (b_1) 62, (b_2) 56, and (b_3) 46 V

In the presence of arc fluctuations, the distribution of particles temperature, velocity and size varies from time to time. Therefore in order to determine the actual distribution for each of the particle characteristics, the average of the distributions in different time steps is calculated. Calculations are done inside a $25 \times 25\ mm^2$ window in front of the gas flow at two different distances from the gun exit. The number of time steps taken into account is chosen in a way that further increasing of time steps would not have a considerable effect on the particle characteristic distributions. The calculated distributions of particle temperature, velocity, and size at 40 and 60 mm from the gun exit are illustrated in Figures 3.13 and 3.14. Figure 3.13 shows that about 40 % of the particles at a distance of 40 mm are in the molten state. By increasing the distance from the gun exit to 60 mm (Figure 3.14), particle temperature drops and the percent of the melted particles decreases to 8%.

Figures 3.13 and 3.14 also show the particles normal velocity distribution at both distances. It is obvious that the particle normal velocity decreases with increasing the distance from the gun exit. Decrease in particle velocity could be explained by the decrease in the plasma gas velocity along the centerline as distance increases. Furthermore, particles size distributions are represented in Figures 3.13 and 3.14. By comparing the size distributions, it can be seen that at the distance of 60 mm particles have slightly smaller diameters. It can be concluded that locating a substrate in a distance closer to the torch exit (40 mm) comparing to 60 mm, gives a higher quality coating.

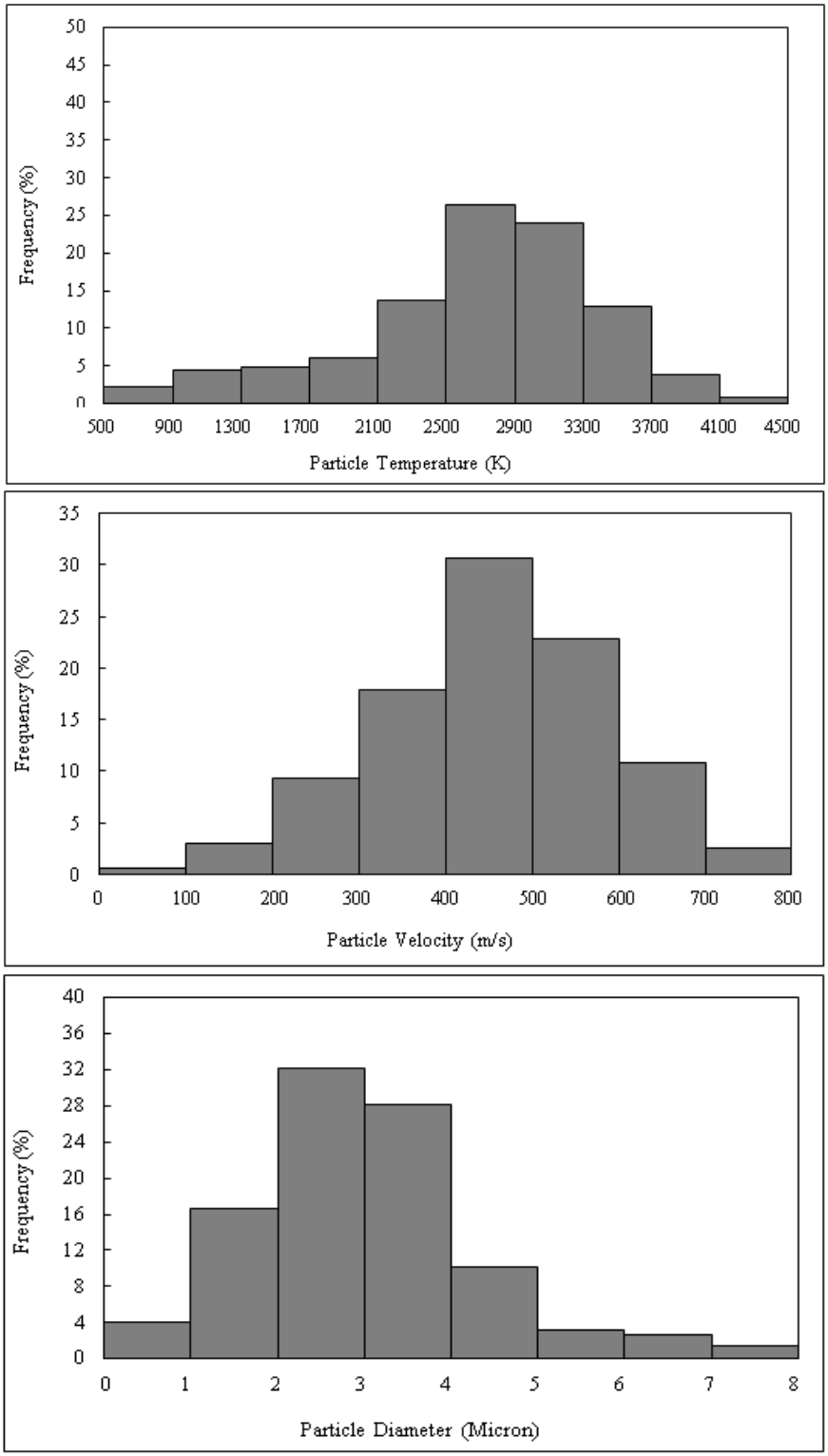

Figure 3.13- Distribution of injected particle temperature, velocity, and size at a distance of 40 mm from the gun exit

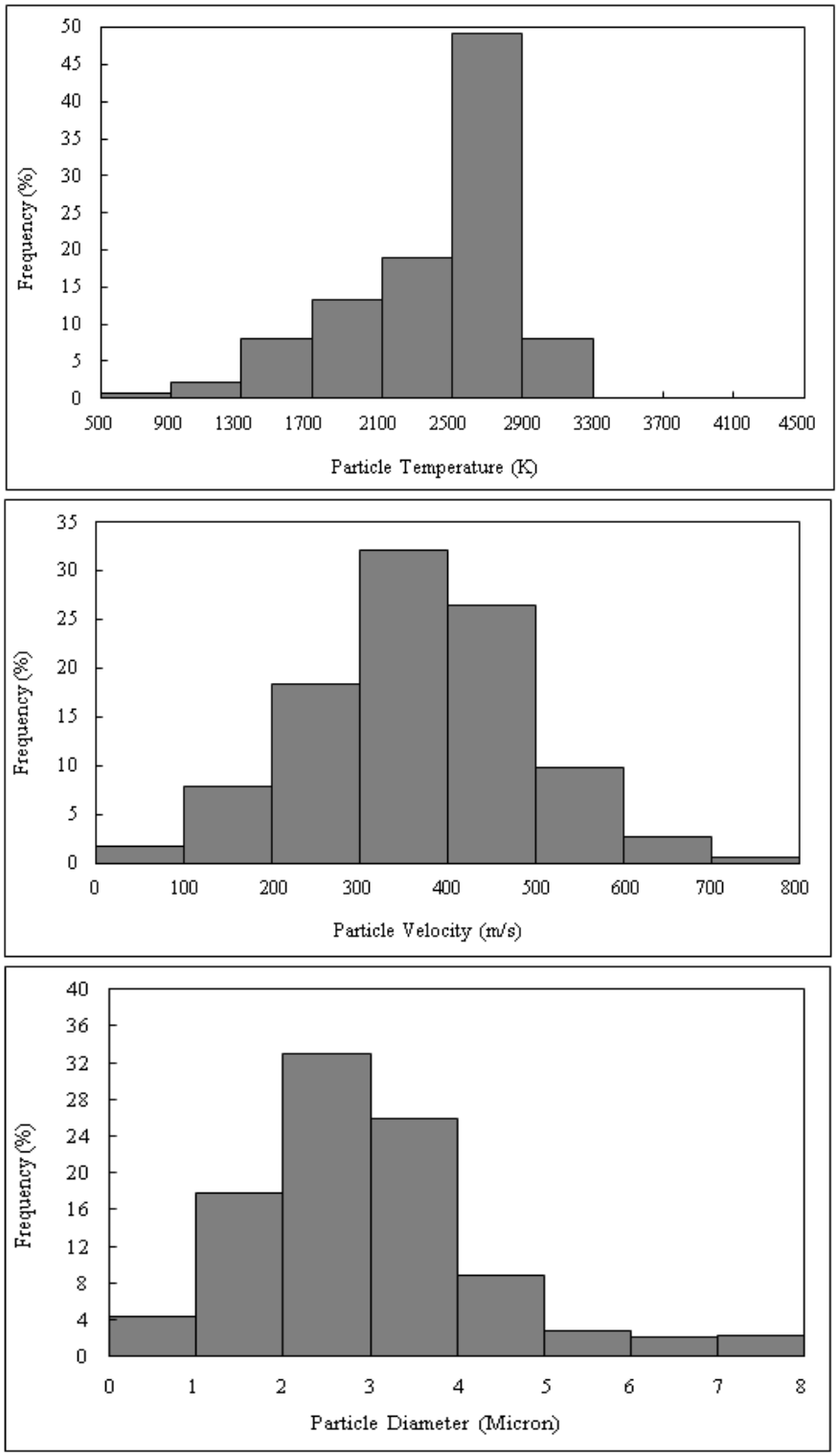

Figure 3.14- Distribution of injected particle temperature, velocity, and size at a distance of 60 mm from the gun exit

3.2.1 Effect of Changing Suspension Feed Rate

In this section, the effect of changing the suspension mass flow rate on the particle trajectories and properties is investigated. Figure 3.15 shows the interaction between the plasma jet and suspension at different mass flow rates of (a) 22, (b) 32, and (c) 42 g/min. To show the plasma gas flow, a temperature isosurface equal to 10400 K is used. Figures 3.16 and 3.17 show the particles and plasma gas temperature and velocity, respectively at 40 mm from the gun exit. It is observed that in cases (b) and (c) comparing to case (a), smaller particles are obtained. The smaller particles are a consequence of a more efficient droplet fragmentation. Another important conclusion is that the number of cold particles is significantly decreased by increasing the suspension mass flow rate.

Figures 3.18, 3.19, and 3.20 represent the sprayed particle temperature, velocity, and diameter distributions, respectively. The values in these figures are calculated from averaging the particles properties in different moments inside a $25 \times 25\, mm^2$ window in front of the gas flow at a distance of 40 mm from the gun exit. It can be observed that in case (b), since the injected particles are closer to the centerline, they gain higher velocities compared to the two other cases. Moreover, the length of the plasma gas decreases by increasing the suspension feed rate. In other words, the plasma jet is cooled down more in case (c) compared to cases (a) and (b).

Comparing different suspension mass flow rates in Figures 3.18, 3.19, and 3.20 shows that the quantity of particles with higher temperature and higher velocity is more in case (b). In addition, increasing the sprayed particles mass flow rate as noted before results in smaller particle size which can be seen in Figure 3.20. The main reason is that larger instabilities on the droplet surface result from the more severe interaction of the droplets with the plasma jet (more penetration).

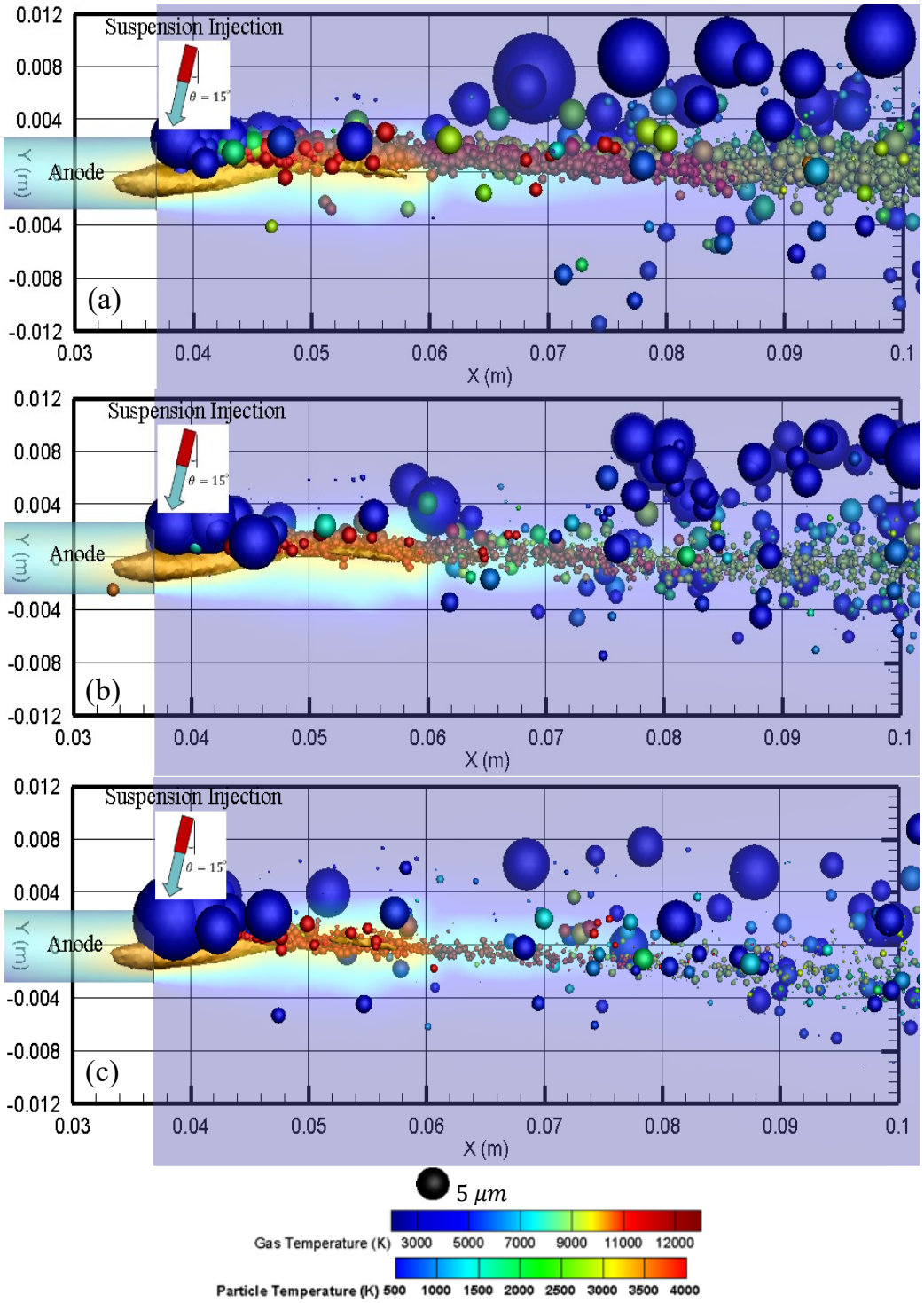

Figure 3.15- Plasma gas and sprayed particles temperatures with suspension feed rates of (a) 22, (b) 32, and (c) 42 g/min

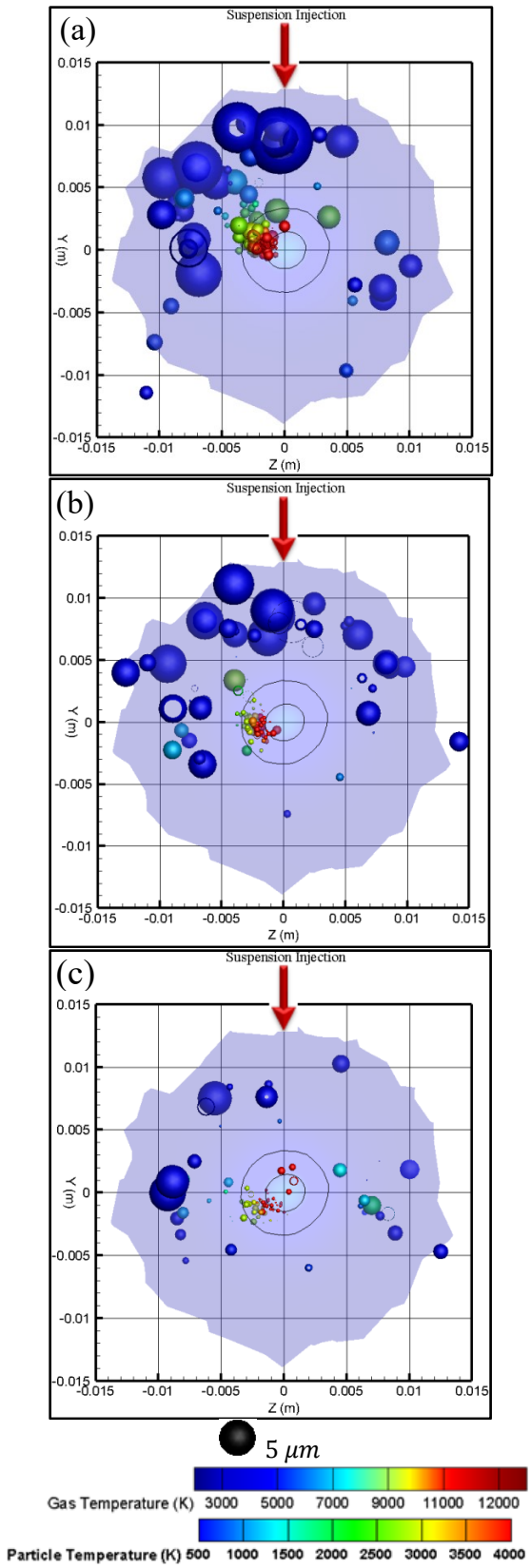

Figure 3.16- Plasma gas and sprayed particles temperatures with suspension feed rates of (a) 22, (b) 32, and (c) 42 g/min at a distance of 40 mm from the gun exit

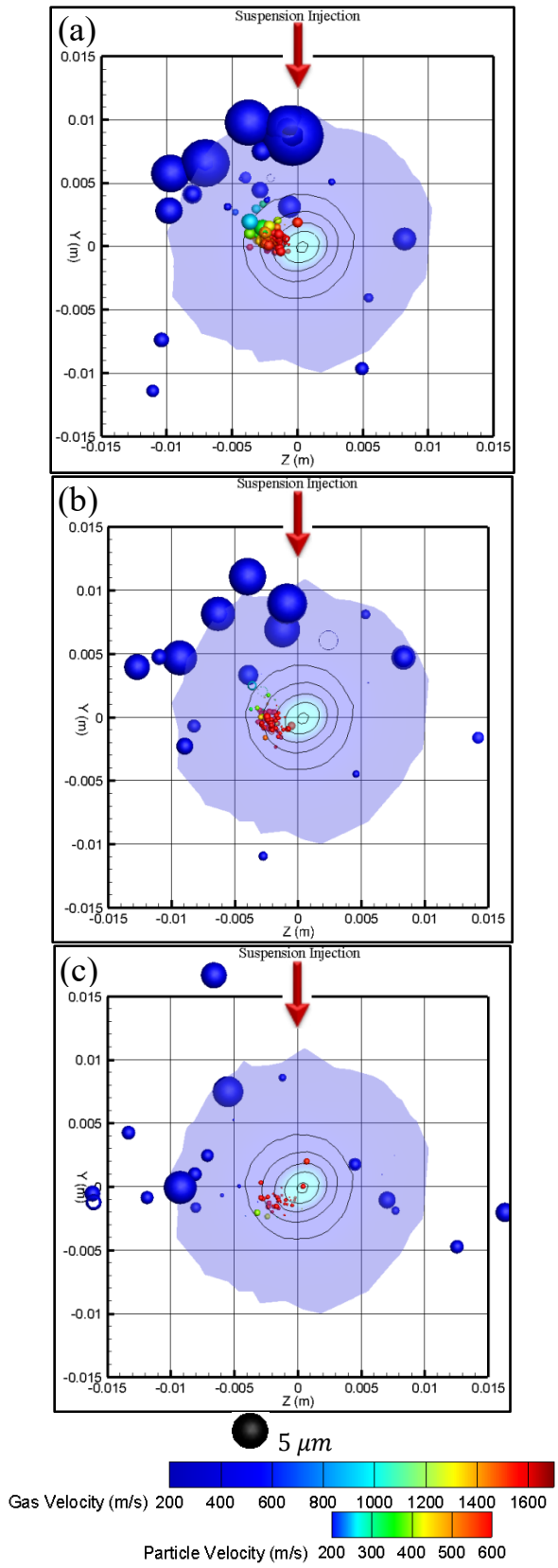

Figure 3.17- Plasma gas and sprayed particles velocities with suspension feed rates of (a) 22, (b) 32, and (c) 42 g/min at a distance of 40 mm from the gun exit

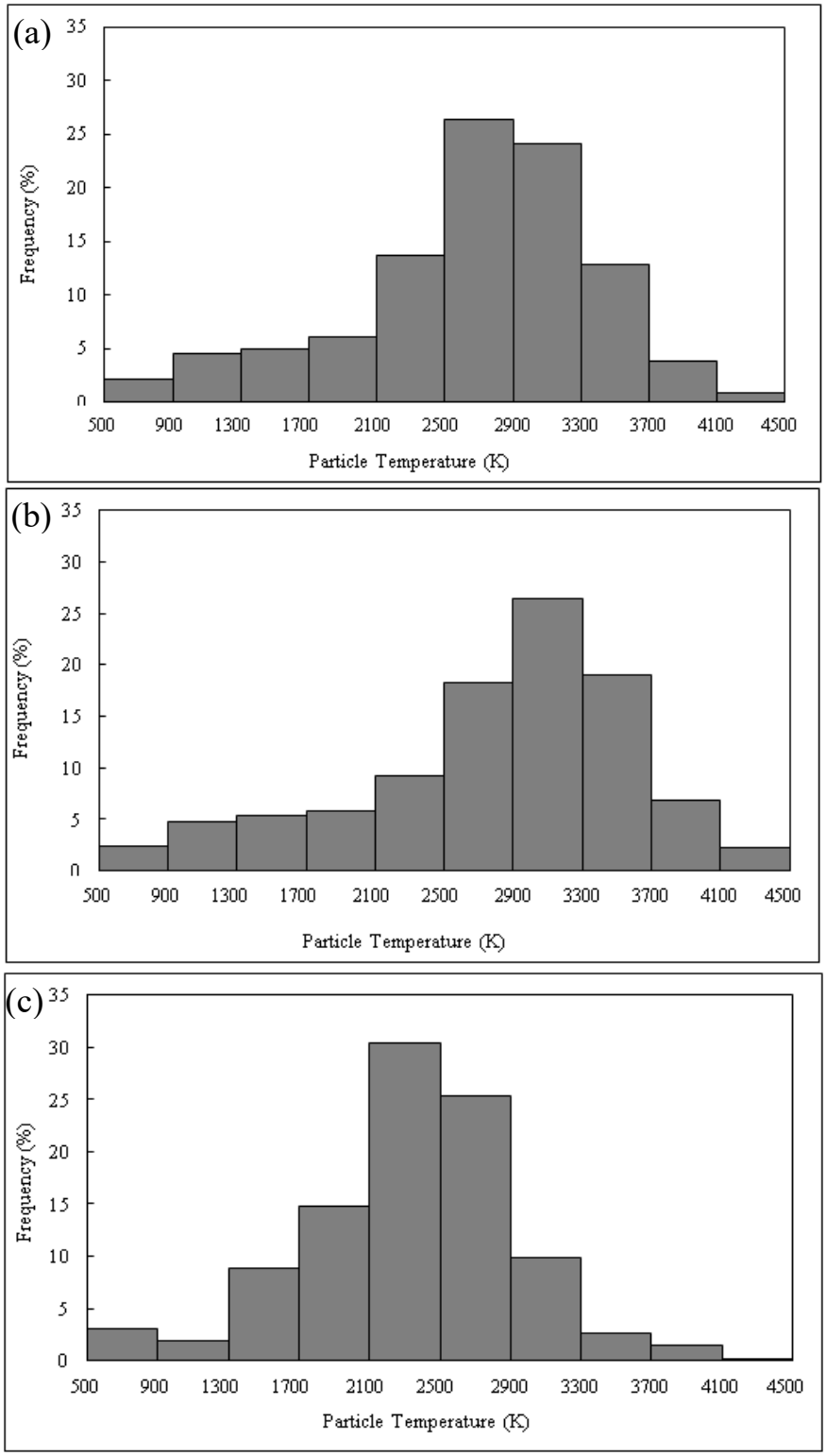

Figure 3.18- Particles temperature located at a distance of 40 mm from the gun exit with feed rates of (a) 22, (b) 32, and (c) 42 g/min

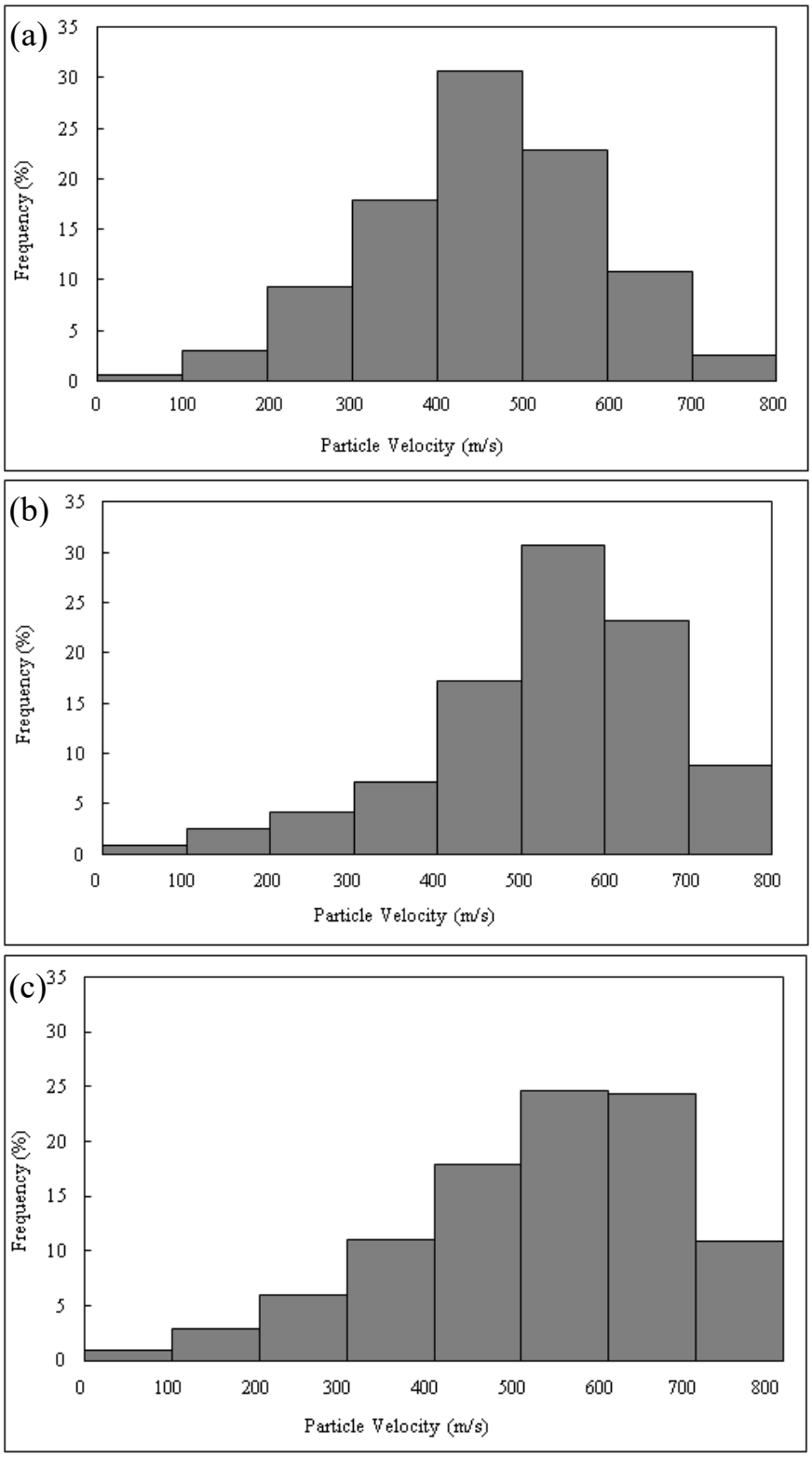

Figure 3.19- Particles velocity located at a distance of 40 mm from the gun exit with feed rates of (a) 22, (b) 32, and (c) 42 g/min

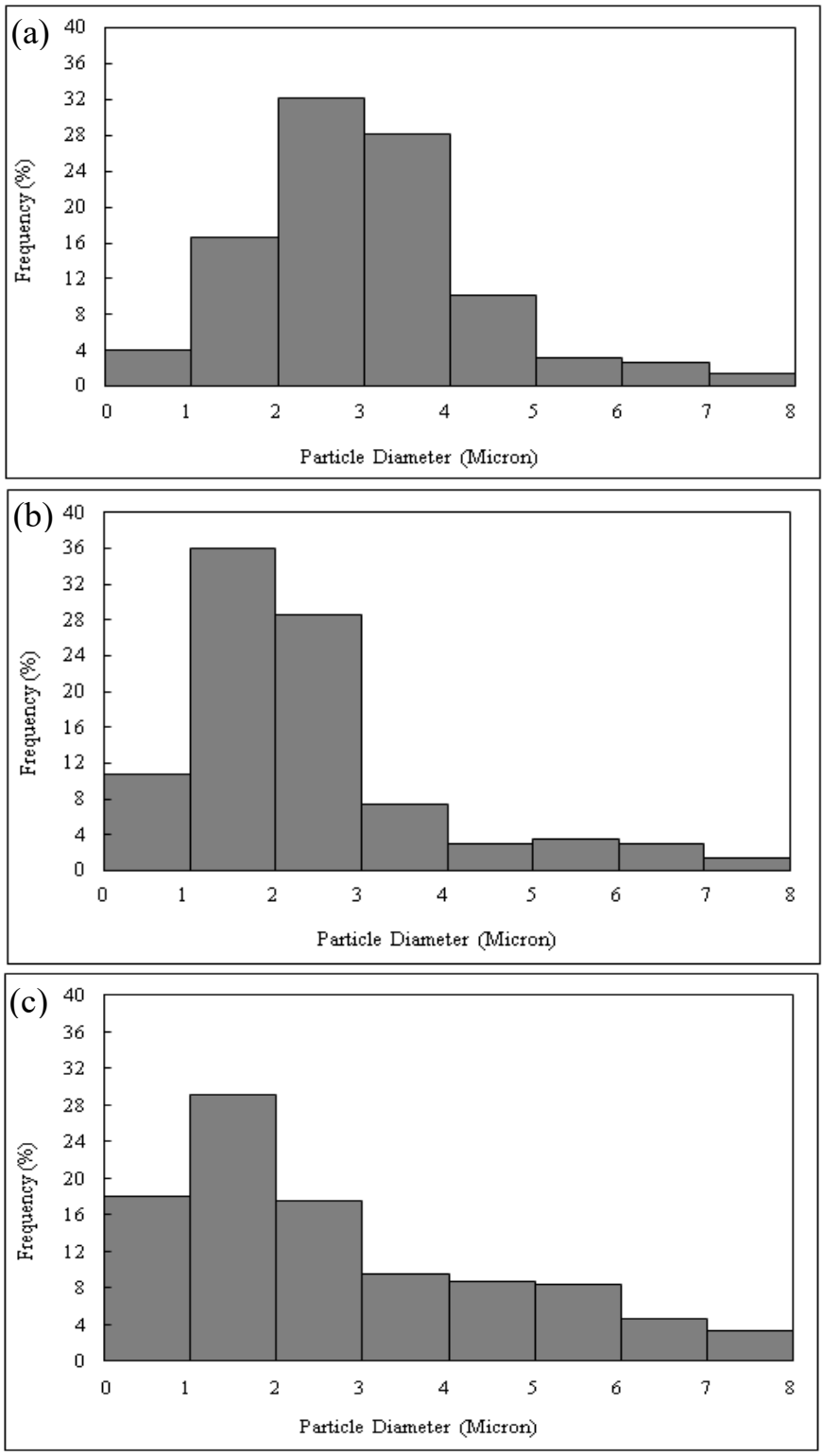

Figure 3.20- Particles diameter located at a distance of 40 mm from the gun exit with feed rates of (a) 22, (b) 32, and (c) 42 g/min

As explained above, in the result of arc fluctuations, the in-flight particle trajectory, temperature, velocity, and size vary with time. Figure 3.21 illustrates the ranges of trajectories obtained with different mass flow rates. Minimum and maximum trajectory lines shown in Figure 3.21, are calculated from the windward trajectory at different moments. It is shown that for high mass flow rates, the suspension sometimes cross the gas flow, and cool it down dramatically. In other words, by increasing the suspension mass flow rate, the average penetration height increases.

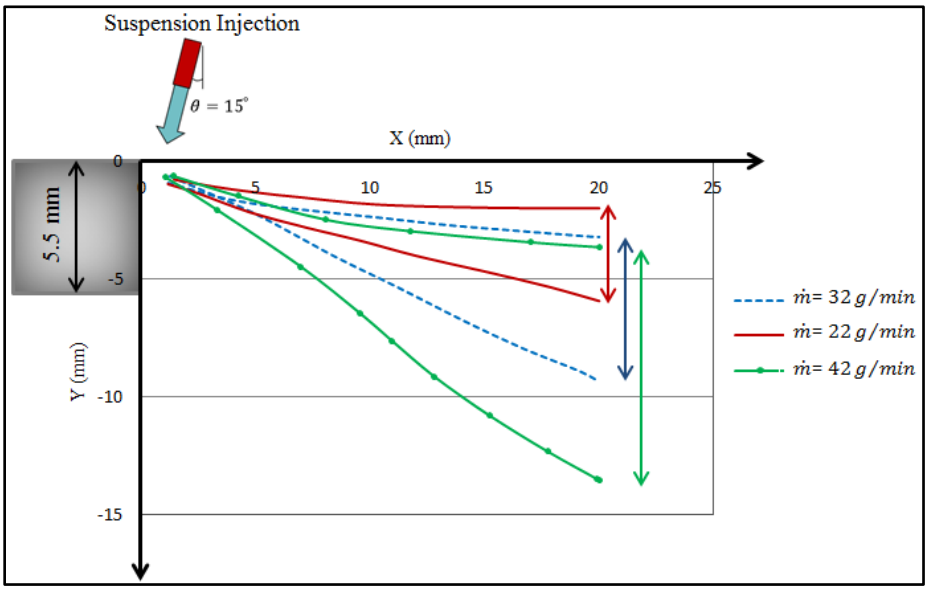

Figure 3.21- Windward trajectory of injected particles with mass flow rates of 22, 32, and 42 g/min

3.2.2 Effect of Eliminating Voltage Fluctuations

In this section, the injection of suspension droplets in the quasi-steady plasma (no voltage fluctuations) is investigated and compared to the results of the transient plasma flow. Here, to generate the plasma heat, a constant volumetric heat source is added to the energy equation. Particles trajectory domain for the new case without voltage fluctuations is shown and compared to the case with arc voltage fluctuations in Figure 3.22. It is evident that in the presence of

voltage fluctuations, the range of trajectories is wider and the penetration is deeper in the plasma jet as in compared to the case with the constant mean voltage.

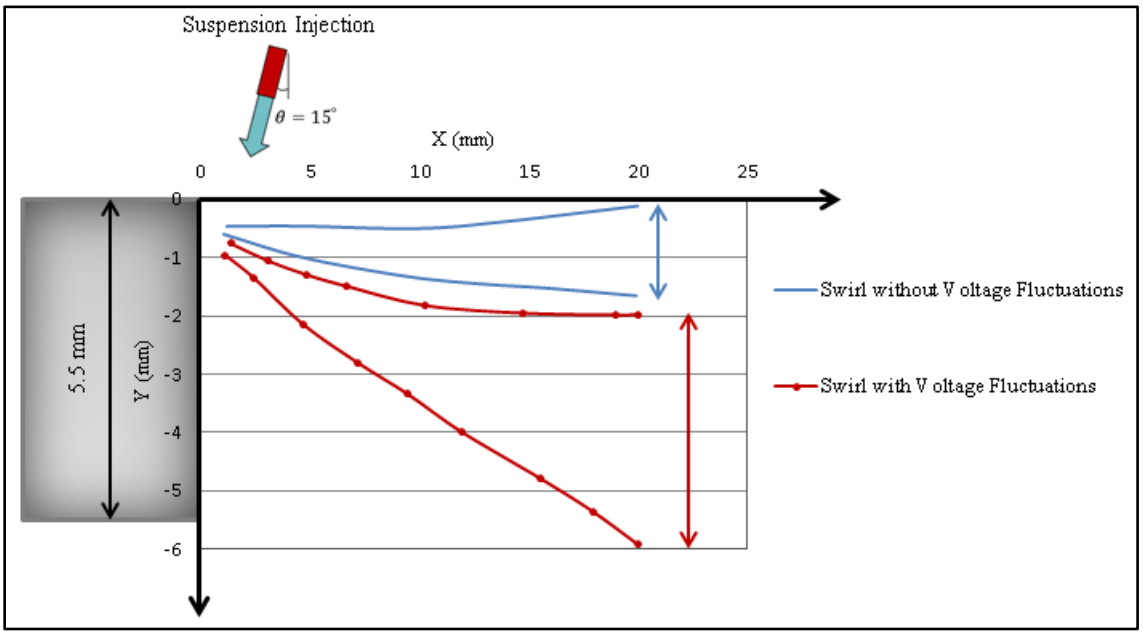

Figure 3.22- Windward trajectory of injected particles in two cases of swirl without voltage fluctuations and swirl with voltage fluctuations (suspension mass flow rate is 22 g/min)

Particle temperature, velocity, and size distributions calculated inside a $25 \times 25\ mm^2$ window across the gas flow at a distance of 40 mm from the gun exit with and without voltage fluctuations are shown in Figure 3.23, 3.24, and 3.25, respectively. In the case of suspension mass flow rate of 22 g/min, the particles have lower temperature and velocity compared to the case with the arc voltage fluctuations and it is the result of weaker penetration.

Furthermore, it could be concluded that in the case of having a constant voltage, the injected particles do not have the chance to penetrate into the centerline of the plasma plume contrary to the case with voltage fluctuations.

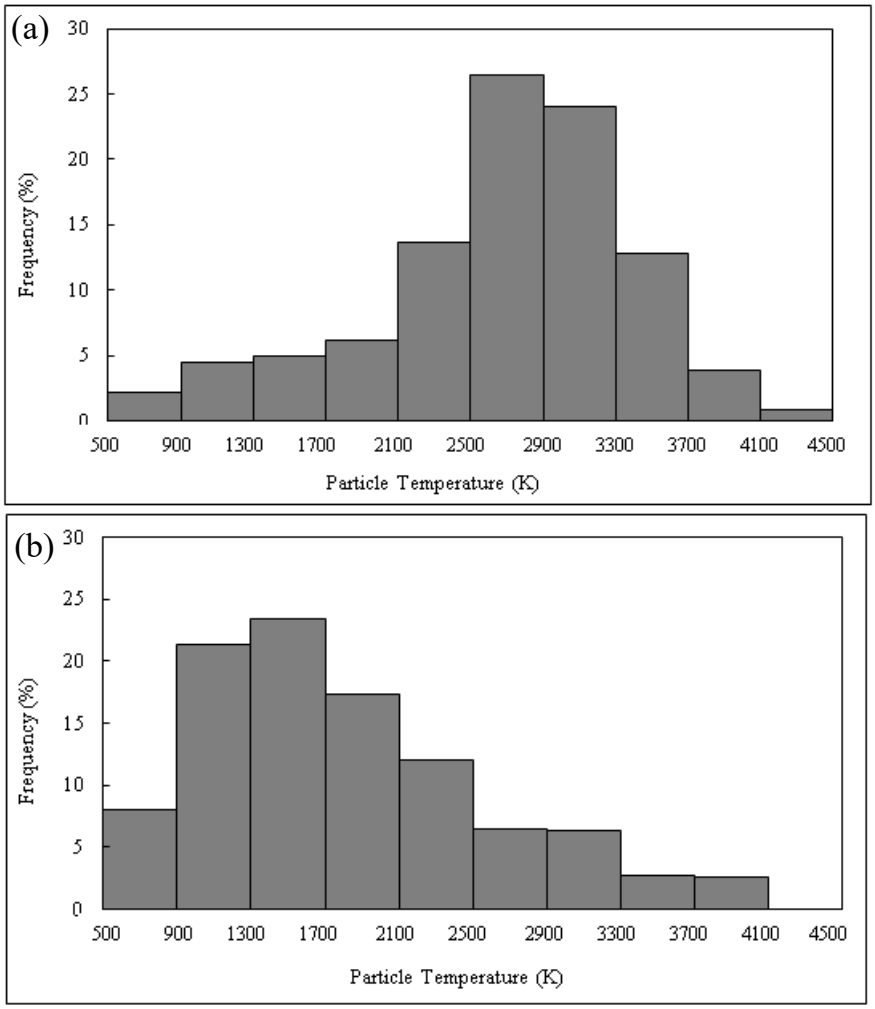

Figure 3.23- Particles temperature located at a distance of 40 mm from the gun exit (a) swirl with voltage fluctuations, (b) swirl without voltage fluctuations

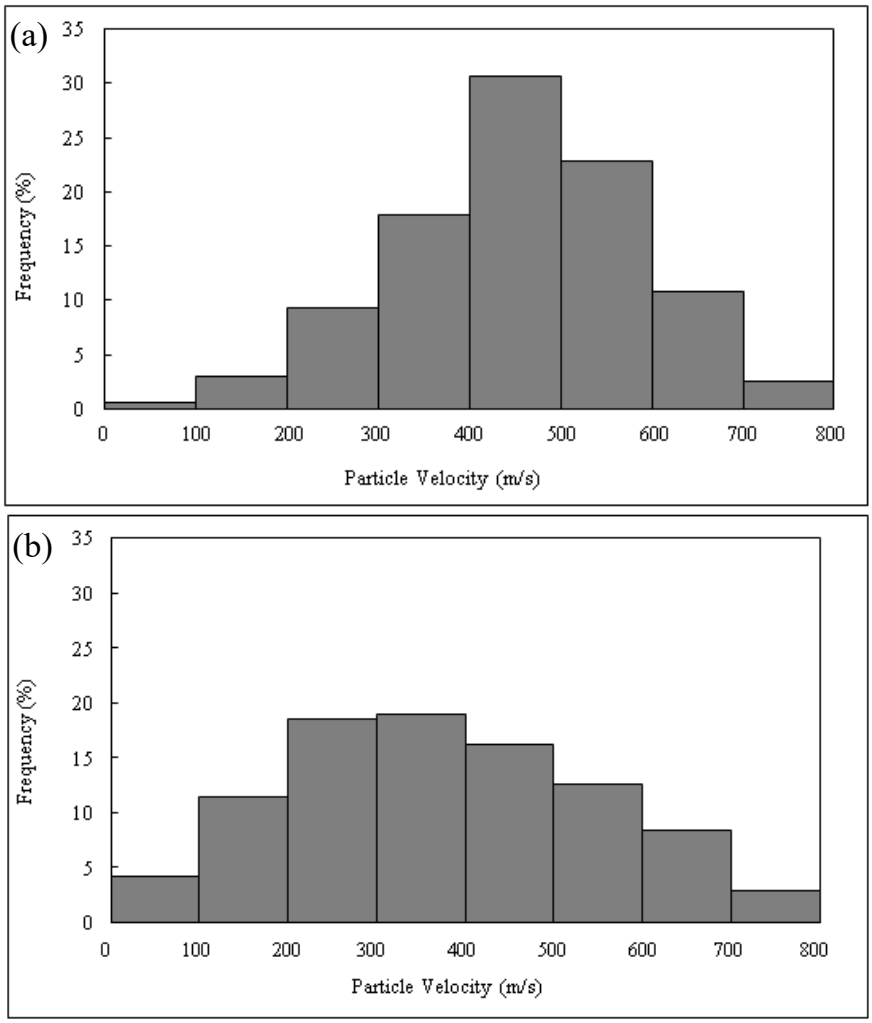

Figure 3.24- Particles velocity located at a distance of 40 mm from the gun exit (a) swirl with voltage fluctuations, (b) swirl without voltage fluctuations

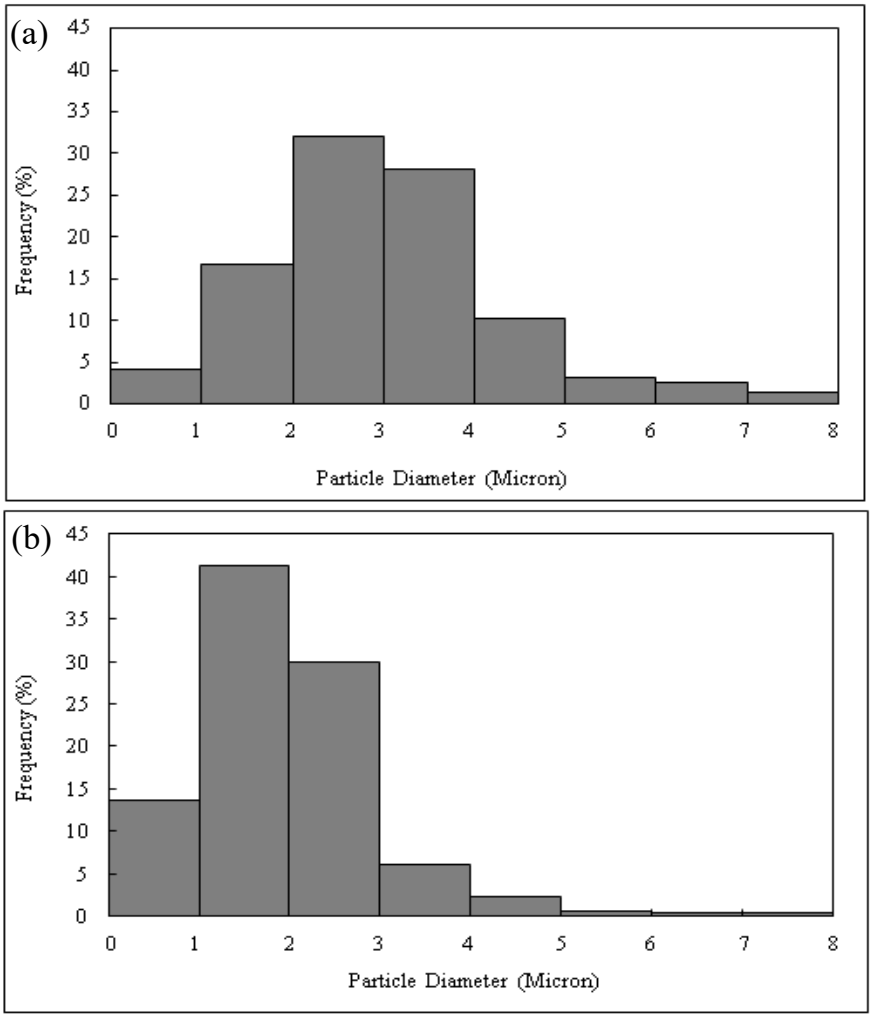

Figure 3.25- Particles diameter located at a distance of 40 mm from the gun exit (a) swirl with voltage fluctuations, (b) swirl without voltage fluctuations

In addition, since the suspension penetration in the case of the quasi-steady plasma jet has less oscillation than that of transient plasma jet, it can be concluded that the particle trajectory, velocity and temperature are more controllable in the quasi-steady case. It is worth mentioning that in the quasi-steady jet by increasing the suspension mass flow rate, the suspension penetration increases and the particles can reach the plasma jet centerline to obtain higher temperature and velocity.

4 Conclusion and Future Work

Overview

In this chapter, a summary and then the conclusion of this study will be presented. Then Future work will be discussed.

A three-dimensional numerical model of suspension plasma spraying has been developed and used to investigate the interaction between the plasma jet and the injected particles. In order to model the plasma heat generation, a time-dependent heat source is introduced inside the plasma torch. In the next step, to simulate the discrete phase a two-way coupled Eulerian-Lagrangian approach is used and the results obtained from the oscillating plasma flow are used to initialize the model.

To model the turbulent flow, Reynolds Stress Model (RSM) which solves the Reynolds shear stresses is applied as the turbulence model. In addition, to model the discrete phase, discrete phase model is used in which the interaction between the plasma gas and in-flight particles is considered. In this way, injected particles are tracked and can exchange their mass, momentum, and energy with the plasma gases. Droplet transport into the plasma gas flow is a very complex phenomenon that comprises droplet penetration, fragmentation, and evaporation. Since the breakup mode here is catastrophic breakup, the KHRT (Kelvin-Helmholtz and Rayleigh-Taylor) model is applied to model the droplet fragmentation. The primary atomization is not considered in this study.

The aim of this research was to develop a more accurate plasma jet model that takes into consideration the arc fluctuations, which are azimuthal fluctuations and axial fluctuations and then investigating the effect of oscillating plasma jet on the injected particle properties.

Moreover, the effect of increasing suspension mass flow rate on the in-flight particles characteristics was investigated. It is observed that by increasing the suspension feed rate, due to deeper penetration, droplets experienced more severe fragmentation resulting in smaller particle size.

Finally, to see the effect of arc voltage fluctuations on the sprayed particle properties, a case with constant voltage called quasi-steady is compared with the case studied in this research. It is found that particle temperature and velocity are lower comparing to the case with voltage fluctuations.

The SPS process is a very complex phenomenon and in order to better understand and model this phenomenon, there are many works that can be done in the future which some of them are listed below,

- Joule effect method used in this study which is one approach to simulate the oscillating plasma jet and its interaction with the sprayed particles has successfully captured the particle properties. However, it would be a good idea to use other approaches and see the differences to have a more accurate plasma jet model.
- LTE assumption is used in this study. However, Non Local Thermodynamic Equilibrium (NLTE) could be considered to model the plasma gas.
- The only fragmentation considered in this study is the secondary breakup. It is better to find a way to apply the primary atomization as well.
- Since there are many factors that affect the sprayed particles such as injected particles diameter, angle of injector, anode erosion, etc. It will give a better understanding if these factors are also examined in the future models.
- Using RSM turbulent model has given reasonable results. However, it is better to test other turbulent models such as LES as well.

References

1. **Fauchais, P.L., Heberlein, J., and Boulos, M.I.,** "Thermal Spray Fundamentals", Springer, 2014.
2. **Hermanek, F.,** "Thermal Spray Terminology and Company Origins", ASM International, Materials Park, OH, 2001.
3. **Fauchais, P., and Vardelle, A.,** "Heat, Mass and Momentum Transfer in Coating Formation by Plasma Spraying", International Journal of Thermal Sciences, vol. 39, pp. 852-870, 2000.
4. **Meillot, E., Vincent, S., Caruyer, C., Caltgirone, J.P., and Damiani, D.,** "From D.C. Time-Dependent Thermal Plasma Generation to Suspension Plasma Spraying Interactions", ASM International, JTTEE5, vol. 18, p. 875–886, 2009.
5. **Duan, Z., and Heberlein, J.,** "Anode Boundary Layer Effects in Plasma Spray Torches", in ASM thermal spray society, Montreal, Quebec, 2000.
6. **Vysohlid, M.,** "Arc Voltage Fluctuations in a Plasma Torch", University of Minnesota, June 2003.
7. **Fazilleau, J., Delbos, C., Rat V., Coudert, J. F., Fauchais, P., and Pateyron, B.,** "Phenomena Involved in Suspension Plasma Spraying Part 1: Suspension Injection and Behavior", Plasma Chemistry and Plasma Processing, vol. 26, no. 4, pp. 371-391, 2006.
8. **Berghaus, J., Marple, B., and Moreau, C.,** "Suspension Plasma Spraying of Nanostructured WC-12Co Coatings", Journal of Thermal Spray Technology, vol. 15, no. 4, pp. 676-681, 2006.

9. **Fauchais, P., Etchart-Salas, R., Delbos, C., Tognonvi, M., Rat, V., Coudert, J F., and Chartier, T.,** "Suspension and Solution Plasma Spraying of Finely Structured Layers: Potential Application to SOFCs", Journal of Physics D: Applied Physics, vol. 40, no. 8, pp. 2394-2406, 2007.

10. **Bisson, JF., Moreau, C., Dorfman, M., Dambra, C., and Mailon, J.,** "Influence of Hydrogen on the Microstructure of Plasma-Sprayed Yttria-Stabilized Zirconia Coatings", J Therm Spray Technol, vol. 14, no. 1, p. 85–90, 2005.

11. **Etchart-Salas, R., Rat, V., Coudert, J.F., Fauchais, P., Caron, N., Wittman, K., and Alexandre, S.,** "Influence of Plasma Instabilities in Ceramic Suspension Plasma Spraying," ASM International, JTTEE5, vol. 16, p. 857–865, 2007.

12. **Samadi, H.,** "A Thick Multilayer Theraml Barrier Coating: Design, Deposition, and Internal Stresses", Stress: The International Journal on the Biology of Stress, 2009.

13. **Jabbari, F., Jadidi, M., Wulthrich, R., and Dolatabadi, A.,** "A Numerical Study of Suspension Injection in Plasma- Spraying Process", ASM International, JTTEE5, vol. 23, pp. 3-13, 2013.

14. **Jadidi, M., Mousavi, M., Moghtadernejad, S., and Dolatabadi, A.,** "A Three-Dimensional Analysis of the Suspension Plasma Spray Impinging on a Flat Substrate", Journal of Thermal Spray Technology, vol. 24, no. 1-2, pp. 11-23, 2014.

15. **Wan, Y. P., Gupta, V., Deng, Q., Sampath, S., Prasad, V., Williamson, R., and Fincke, J. R.,** "Modeling and Visualization of Plasma Spraying of Functionally Graded Materials and Its Application to the Optimization of Spray Conditions", ASM International, JTTEE5, vol. 10, pp. 382-389, 2000.

16. **Khelfi, D., El-hadj, a Abdellah., and Ait-Messaoudene, N.,** "Modeling of a 3D Plasma Thermal Spraying and the Effect of the Particle Injection Angle", Revue des Energies Renouvelables CISM'08 Oum El Bouaghi, p. 205 – 216, 2008.
17. **Boussagol, A., Mariaux.G., Legros, E., Vardelle, A., and Nylen, P.,** "3-D Modeling of a D.C. Plasma Jet Using Different Commercial CFD Codes", in Proc. 14th Int. Symp. On Plasma Chemistry, Orleans, France, 2000.
18. **Williamson, R L., Fincke, J R., and Chang, C H.,** "A Computational Examination of the Sources of Statistical Variance in Particle Parameters During Thermal Plasma Spraying", Plasma Chemistry and Plasma Processing, vol. 20, no. 3, 2000.
19. **Cheng, Kai., Chen, Xi., and Pan, Wenxia.,** "Comparison of Laminar and Turbulent Thermal Plasma Jet Characteristics- A Modeling Study", Plasma Chem Plasma Process, vol. 26, p. 211–235, 2006.
20. **Fincke, J. R., Crawford, D. M., Snyder, S. C., Swank, W. D., Haggard, D. C., and Williamson, R. L.,** "Entrainment in High-Velocity, High-Temperature Plasma Jets. Part I: Experimental results", Int. J. Heat and Mass Transfer, vol. 46, 2003.
21. **Pourang, K., Moreau, C., and Dolatabadi, A.,**"A Three-Dimensional Analysis of the Suspension Plasma Spray Impinging on a Curved Substrate", ASM International, vol. 6, pp. 223 - 228, 2015
22. **Eichert, P., Imbert, M., and Coddet, C.,** "Numerical Study of an ArH2 Gas Mixture Flowing Inside and Outside a de Plasma Torch", ASM International, JTTEE5, vol. 7, pp. 505-512, 1998.

23. **Huang, R., Fuckanuma, H., Uesugi, Y., and Tanaka, Y.,** "Simulation of Arc Root Fluctuation in a DC Non-Transferred Plasma Torch with Three Dimensional Modeling", ASM International, JYYEES, vol. 21, pp. 636-643, 2011.
24. **Safaei Ardakani, E., and Mostaghimi, J.,** "Arc Fluctuation Modeling in Non-Transferred Direct Current Argon Plasma Torch", in 22nd International Symposium on Plasma Chemistry, Antwerp, Belgium, 2015.
25. **Trelles, J P., Pfender, E., and Heberlein, J.,** "Multiscale Finite Element Modeling of Arc Dynamics in a DC Plasma Torch", Plasma Chem, Plasma Process, vol. 26, no. 6, pp. 557-575, 2006.
26. **Moreau, E., Chazelas, C., Mariaux, G., and Vardelle, A.,** "Modeling the Restrike Mode Operation of a DC Plasma Spray Torch", ASM International, JTTEE5, vol. 15, pp. 524-530, 2006.
27. **Meillot, E., Guenadou, D., and Bourgeois, C.,** "Three-Dimension and Transient D.C. Plasma Flow Modeling", Plasma Chem Plasma Process, vol. 28, p. 69–84, 2008.
28. **Duan, Z. and Heberlein, J.,** "Arc Instabilities in a Plasma Spray Torch", Journal of Thermal Spray Technology, vol. 11, no. March, pp. 44-51, 2002.
29. **Remesh, K., Yu, S.C.M., Ng, H.W., and Berndt, C.C.,** "Computational Study and Experimental Comparison of the In-Flight Particle Behavior for an External Injection Plasma", ASM International, JTTEE5, vol. 12, pp. 508-522, 2003.
30. **Shan, Y., Coyle, T., and Mostaghimi, J.,** "Numerical Simulation of Droplet Breakup and Collision in the Solution Precursor Plasma Spraying", Journal of Thermal Spray Technology, vol. 16, no. 5-6, pp. 698-704, 2007.

31. **Vincent, S., Balmigere, G., Caruyer, C., Meillot, E., and Caltagirone, J.P.,** "Contribution to the mModeling of the Interaction between a Plasma Flow and a Liquid Jet", Surface and Coatings Technology, vol. 203, no. 15, pp. 2162-2171, 2009.

32. **ANSYS, Inc.,** "ANSYS FLUENT Theory Guide", 2011

33. **Morsi, S. A. and Alexander, A. J.,** "An Investigation of Particle Trajectories in Two-Phase Flow Systems", Journal of Fluid Mechanics, Vol. 55(2), pp 193–208, 1972.

34. **Ranz, W. E., and Marshall, W. R.,** "Evaporation from Drops, Part I", Chem. Eng. Prog., vol. 48, no. 3, pp. 141-146, March 1952.

35. **Ranz, W. E., and Marshall, W. R.,** "Evaporation from Drops, Part I and Part II", Chem. Eng. Prog., vol. 48, no. 4, pp. 173-180, April 1952.

36. **Plich, M., and Erdman, C. A.,** "Use of Breakup Time Data and Velocity History Data to Predict the Maximum Size of Stable Fragments for Acceleration-Induced Breakup of a Liquid Drop", Int. J. Multiphase Flow, vol. 13, no. 6, pp. 741-757, 1987.

37. **Ashgriz, N.,** "Handbook of Atomization and Sprays- Theory and Applications", 2011.

38. **Sulzer Metco (US) Inc.,** "3MBM/3MBH Plasma Spray Gun Manual- Plasma Spraying", Westbury, NY 11590, 2008.

39. **Kang, C., Ng, H., and Yu, S.,** "Comparative Study of Plasma Spray Flow Fields and Particle Behavior Near to Flat Inclined Substrates", Plasma Chem Plasma Process, vol. 26, pp. 149-175, 2006.

40. **Planche, M. P.,** "Experimental Study of Fluctuating Plasma Jets", Ph.D. Thesis, University of Limoges, France, 1995.

41. **Betoule, O.,** "Relationships between the Distributions of Particle Velocity and Temperature and Coating Properties", Ph.D. Thesis, University of Limoges, France, 1994.